

## Ground-based astrometry with wide field imagers

### V. Application to near-infrared detectors: HAWK-I@VLT/ESO<sup>★,★★</sup>

M. Libralato<sup>1,2,3,★★★</sup>, A. Bellini<sup>2</sup>, L. R. Bedin<sup>3</sup>, G. Piotto<sup>1,3</sup>, I. Platais<sup>4</sup>, M. Kissler-Patig<sup>5,6</sup>, and A. P. Milone<sup>7</sup>

<sup>1</sup> Dipartimento di Fisica e Astronomia, Università di Padova, Vicolo dell'Osservatorio 3, 35122 Padova, Italy  
e-mail: [giampaolo.piotto;mattia.libralato]@studenti.unipd.it

<sup>2</sup> Space Telescope Science Institute, 3700 San Martin Drive, Baltimore MD-21218, USA  
e-mail: bellini@stsci.edu

<sup>3</sup> INAF-Osservatorio Astronomico di Padova, Vicolo dell'Osservatorio 5, 35122 Padova, Italy  
e-mail: luigi.bedin@oapd.inaf.it

<sup>4</sup> Department of Physics and Astronomy, The Johns Hopkins University, Baltimore MD-21218, USA  
e-mail: imants@pha.jhu.edu

<sup>5</sup> Gemini Observatory, N. Aohoku place 670, Hilo, Hawaii 96720, USA  
e-mail: mkissler@gemini.edu

<sup>6</sup> European Southern Observatory, Karl-Schwarzschild-Str. 2, Garching, 85748 München, Germany

<sup>7</sup> Research School of Astronomy and Astrophysics, The Australian National University, Cotter Road, Weston ACT 2611, Australia  
e-mail: milone@mso.anu.edu.au

Received 11 June 2013 / Accepted 18 December 2013

#### ABSTRACT

High-precision astrometry requires accurate point-spread function modeling and accurate geometric-distortion corrections. This paper demonstrates that it is possible to achieve both requirements with data collected at the high acuity wide-field *K*-band imager (HAWK-I), a wide-field imager installed at the Nasmyth focus of UT4/VLT ESO 8 m telescope. Our final astrometric precision reaches  $\sim 3$  mas per coordinate for a well-exposed star in a single image with a systematic error less than 0.1 mas. We constructed calibrated astro-photometric catalogs and atlases of seven fields: the Baade's window, NGC 6656, NGC 6121, NGC 6822, NGC 6388, NGC 104, and the *James Webb* Space Telescope calibration field (in the Large Magellanic Cloud). We make these catalogs and images electronically available to the community. Furthermore, as a demonstration of the efficacy of our approach, we combined archival material taken with the optical wide-field imager at the MPI/ESO 2.2 m with HAWK-I observations. We showed that we are able to achieve an excellent separation between cluster members and field objects for NGC 6656 and NGC 6121 with a time base-line of about 8 years. Using both HST and HAWK-I data, we also study the radial distribution of the SGB populations in NGC 6656 and conclude that the radial trend is flat within our uncertainty. We also provide membership probabilities for most of the stars in NGC 6656 and NGC 6121 catalogs and estimate membership for the published variable stars in these two fields.

**Key words.** instrumentation: detectors – astrometry – techniques: image processing – Galaxy: bulge – globular clusters: general – proper motions

### 1. Introduction

Multiple fields within astronomy are driving the execution of larger and yet larger surveys of the sky. Over the last two decades, this scientific need has stimulated the construction of instruments equipped with mosaics of large-format digital detectors for wide-field imaging at both the optical and near-infrared (NIR) wavelengths. The most recent generation of these wide-field imagers now competes with the older technology of Schmidt telescope and photographic plates in terms of number of resolution elements on sky but does so with order-of-magnitude greater sensitivity and efficiency.

A list of some widely-used wide-field imagers was given by Anderson et al. (2006, hereafter Paper I). Since then, however,

many wide-field imagers have been upgraded or decommissioned, and additional new wide-field imagers have begun their operations. In the top-half of Table 1, we provide a brief list of the major operative wide-field imagers on 3 m+ telescopes (we also included the WFI@2.2 m MPI/ESO as reference).

In addition, two wide-field imagers mounted on 1 m telescopes should be mentioned. The LaSilla-QUEST Variability survey is a project that uses the ESO 1.0-m Schmidt Telescope at the La Silla Observatory of the European Southern Observatory in Chile with the new large area QUEST camera. It is a mosaic of  $112\,600 \times 2400$  pixels CCDs covering a field of view (FoV) of about  $4.6^\circ \times 3.6^\circ$ . The camera, commissioned in early 2009 has been built at the Yale and Indiana Universities. La Silla-QUEST survey is expected to cover about 1000 square degrees per night repeated with a 2-day cadence (Hadjijska et al. 2012).

The Panoramic Survey Telescope and Rapid Response System (Pan-STARRS) also is of great interest for the astronomical community. The Pan-STARRS survey will cover the sky using wide-field facilities and provide astrometric and photometric

\* Catalogs, fortran code, and distortion maps are only available at the CDS via anonymous ftp to [cdsarc.u-strasbg.fr](http://cdsarc.u-strasbg.fr) (130.79.128.5) or via

<http://cdsarc.u-strasbg.fr/viz-bin/qcat?J/A+A/563/A80>

\*\* Based on observations with the 8 m VLT ESO telescope.

\*\*\* Visiting Ph.D. Student at STScI under the 2013 DDRF program.

**Table 1.** List of the major operative wide-field imagers on 3 m+ telescopes.

Name	Telescope	Detectors	Pixel scale ["/pixel]	FoV
OPTICAL REGIME				
WFI	2.2 m MPI/ESO	8 × (2048 × 4096)	0.238	34' × 33'
Prime Focus Camera	<i>William Herschel</i> Telescope	2 × (2048 × 4100)	0.24	16'2 × 16'2
LBC (blue and red)	LBT	4 × (2048 × 4608)	0.23	23' × 23'
Suprime-Cam	Subaru Telescope	10 × (2048 × 4096)	0.202	34' × 27'
MOSA	KPNO Mayall 4 m	8 × (2048 × 4096)	0.26	36' × 36'
LAICA	Calar Alto 3.5 m Telescope	4 × (4096 × 4096)	0.225	44'36 × 44'36
MegaCam	CFHT	36 × (2048 × 4612)	0.187	57'6 × 56'4
OmegaCam	VST	32 × (2048 × 4102)	0.21	60' × 60'
DECam	CTIO Blanco 4 m	62 × (2048 × 4096) + 12 × (2048 × 2048)	0.27	132' × 132'
NIR REGIME				
GSAOI	Gemini	4 × (2048 × 2048)	0.02	1'42 × 1'42
HAWK-I	VLT	4 × (2048 × 2048)	0.106	7'5 × 7'5
ISPI	CTIO Blanco 4 m	1 × (2048 × 2048)	0.3	10'25 × 10'25
FourStar	<i>Magellan</i>	4 × (2048 × 2048)	0.159	10'8 × 10'8
WFCAM	UKIRT	4 × (2048 × 2048)	0.4	12'6 × 12'6
Omega2000	Calar Alto 3.5 m Telescope	4 × (2048 × 2048)	0.45	15'4 × 15'4
WIRCAM	CFHT	4 × (2048 × 2048)	0.3	20'5 × 20'5
NEWFIRM	CTIO Blanco 4 m	4 × (2048 × 2048)	0.4	27'6 × 27'6
VIRCAM	VISTA	16 × (2048 × 2048)	0.339	35'4 × 35'4

**Notes.** The WFI@2.2 m MPI/ESO has been included as reference.

data for all observed objects. The first Pan-STARRS telescope, PS1, is located at the summit of Haleakala on Maui, Hawaii and began full time science observations on May 13, 2010 (Kaiser et al. 2010). With its 1.8 m primary mirror, it covers a FoV of  $\sim 7$  square degrees.

Among wide-field imagers planned for the future, the Large Synoptic Survey Telescope (LSST)<sup>1</sup> represents the most significant step forward for wide-field imagers in modern astrophysics. It will be a 8.4 m wide-field ground-based telescope with a FoV of about 9.6 square degrees. With its 189 4k × 4k CCDs, it will observe over 20 000 square degrees of the southern sky in six optical bands. Construction operations should begin in 2014; the survey will be taken in 2021.

While a great number of papers have presented photometry obtained with these facilities over the last decade, their astrometric potential has remained largely unexploited. Our team is committed in pushing the astrometric capabilities of wide-field imagers to their limits. Therefore, we have begun to publish in this Journal a series of papers on Ground-based astrometry with wide field imagers. In Paper I, we developed and applied our tools to data collected with the WFI@2.2 m MPI/ESO telescope. The techniques used in Paper II (Yadav et al. 2008) and Paper III (Bellini et al. 2009) produced astro-photometric catalogs and proper motions of the open cluster M 67 and of the globular cluster NGC 5139, respectively. In Paper IV (Bellini & Bedin 2010), we applied the technique to the wide-field camera on the blue focus of the LBC@LBT 2 × 8.4 m.

In this paper, we turn our attention to wide-field imagers equipped with NIR detectors. Indeed, the pioneering work of 2MASS has shown the great potential of these instruments (Skrutskie et al. 2006). The number and the quality of NIR detectors has improved considerably since then. New generations of 2k × 2k arrays are now mounted at the foci of various telescopes (bottom-half of Table 1).

These wide-field imagers enable wide surveys, such as the VISTA variables in the Via Lactea (VVV, Minniti et al. 2010). The VVV is monitoring the Bulge and the Disk of the Galaxy. The survey will map 562 square degrees over 5 years (2010–2014) and give NIR photometry in  $Z$ ,  $Y$ ,  $J$ ,  $H$ , and  $K_S$  bands. The first data set of the VVV project has already been released to the community (Saito et al. 2012). It contains 348 individual pointings of the Bulge and the Disk, taken in 2010 with  $\sim 10^8$  stars observed in all filters. Typically, the declared astrometric precisions vary from  $\sim 25$  mas for a star with  $K_S = 15$ , to  $\sim 175$  mas for a star with  $K_S = 18$  mag.

Ground-based telescopes are not alone in focusing their attention on this kind of detector. The *James Webb* Space Telescope (JWST) will be a 6.5 m space telescope optimized for the infrared regime. It will orbit around the Earth's second Lagrange point (L2), and it will provide imaging and spectroscopic data. The wide-field imager, NIRCAM, will be made up by a short- (0.6–2.3  $\mu\text{m}$ ) and a long-wavelength (2.4–5.0  $\mu\text{m}$ ) channel with a FoV of  $2^\circ 2 \times 4^\circ 4$  each.

In this paper, we explore the astrometric performance of the HAWK-I@VLT facility and provide astrometric catalogs (together with stacked images) of seven dense stellar fields along with the tools required to correct any observed field for geometric distortion. We adopt the UCAC 4 catalog (Zacharias et al. 2013) as a reference frame to determine the linear terms of the distortion and to put all the objects on the International Celestial Reference System but at the epoch of our observations.

The paper is organized as follows: in Sect. 2, we briefly describe the instrument. Section 3 presents the observations. Section 4 describes the tools developed to extract the position and flux of the sources. In Sect. 5, we derive our geometric-distortion solution. In Sect. 6, we discuss the periodic feature of the residual highlighted during the geometric-distortion correction and give a possible explanation. Sections 7 and 8 describe how we removed the point-spread function (PSF) artefacts from the catalogs and the photometric calibration, respectively. Section 9 shows some possible applications of our calibrations.

<sup>1</sup> <http://www.lsst.org/lsst/>

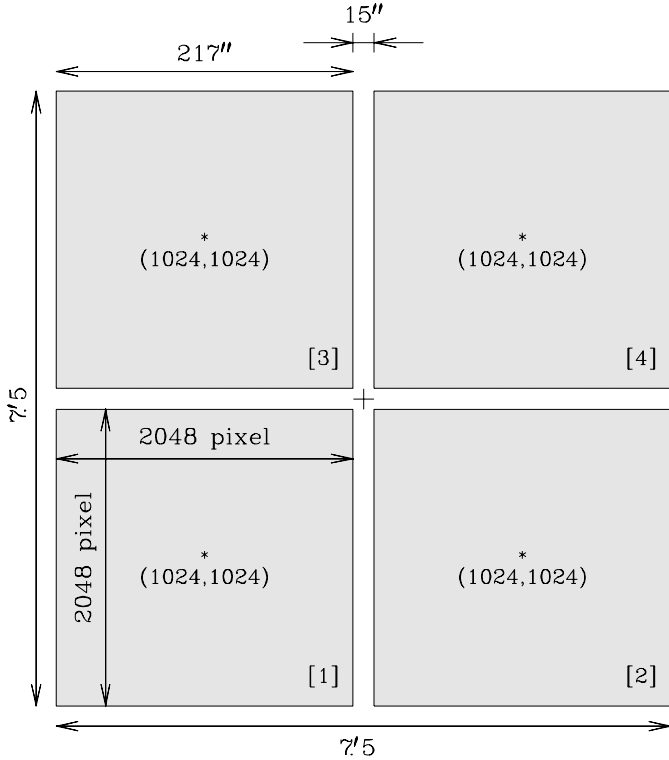


**Fig. 1.** HAWK-I layout. The labels give the dimensions in arcsec and arcmin (and in pixels) of the four detectors and of the gaps. Numbers in square brackets label the chip denomination used in this work (note that the choice is different from that of Fig. 9 of Kissler-Patig et al. 2008). In each chip, we indicate the coordinate of the chip center. This is also the reference position that we used while computing the polynomial correction described in Sect. 5.1. The black asterisk in the middle shows the center of the field of view in a single exposure that we used in Fig. 2.

Finally, we describe the catalogs that we release with this paper in Sect. 10.

## 2. HAWK-I@VLT

An exhaustive description of HAWK-I is given in Kissler-Patig et al. (2008). Here, we only provide a brief summary.

The HAWK-I focal plane is equipped with a mosaic of four  $2048 \times 2048$  pixels Rockwell HgCdTe Molecular Beam Epitaxy HAWAII-2RG arrays. The pixel-scale (Kissler-Patig et al. 2008) is about  $106 \text{ mas pixel}^{-1}$ , resulting in a total FoV of about  $7.5 \times 7.5$  (with gaps of  $\sim 15''$  between the detectors). A sketched outline of the HAWK-I FoV layout is shown in Fig. 1. The detectors and the filter wheel unit are connected to the second stage of the Closed Cycle Cooler and operated at a temperature close to  $75\text{--}80 \text{ K}$ . The remaining parts of the instrument are cooled to a temperature below  $140 \text{ K}$ . The acquisition system is based on the Infrared Array Control Electronics system (IRACE) developed at ESO. HAWK-I also is designed to work with a ground-layer adaptive optics module (GRAAL) as part of the Adaptive Optics Facility (Arsenault et al. 2006) for the VLT (scheduled to be installed in the second half of 2014). HAWK-I broad band filters follow the Mauna Kea Observatory specification.

## 3. Observations

In Table 2 we provide a detailed list of the observations.

All of the HAWK-I images used here were collected during the instrument commissioning, when several fields were

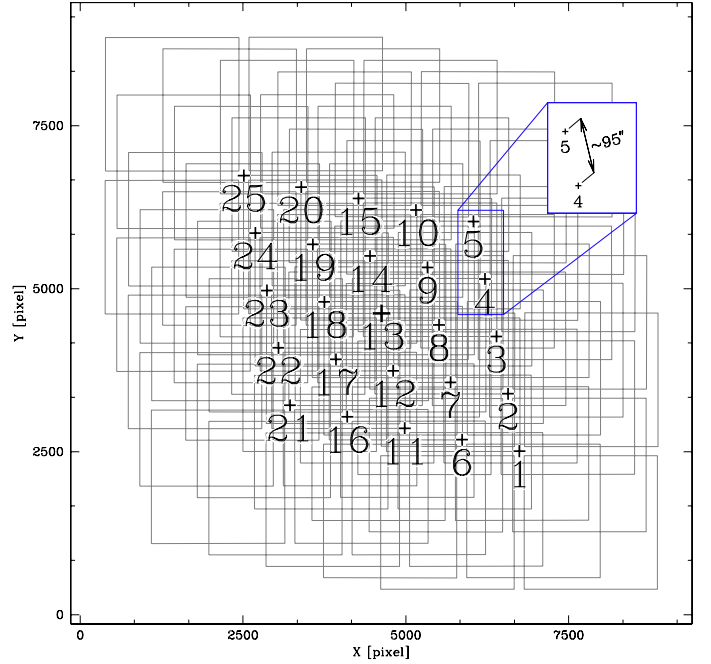


**Fig. 2.** Outline of the relative positions of pointings in our adopted dither-pattern strategy. The 25 images are organized in a  $5 \times 5$  array, where the center of the field falls in the central position 13. The other pointings are taken in a way that the gaps between the four detectors never cover the same point of sky more than once. The 25 images were designed for astrometric purposes allowing stars in frame 13 to be imaged in as many different locations of the detectors as possible. This enables us to self-calibrate the geometric distortion. The zoom-in in the blue panel shows an example of the adopted dither between two pointings. As described in Table 2, the shift step can change from field to field.

observed with the aim of determining an average optical geometric-distortion solution for HAWK-I and for monitoring its stability in the short- and mid-term.

To this end, the fields were observed with an observing strategy that would enable a self-calibration of the distortion. Briefly, the strategy consists of observing a given patch of sky in as many different parts of the detectors as possible. Each observing block (OB) is organized in a run of 25 consecutive images. The exposure time for each image was the integration time (DIT in s) times the number of individual integrations (NDIT). Figure 2 shows the outline of the adopted dither-pattern strategy<sup>2</sup>.

Important by-products of this effort are astrometric standard fields (i.e., catalogs of distortion-free positions of stars), which in principle could be pointed by HAWK-I anytime in the future to efficiently assess whether the distortion has varied and by how much. Furthermore, these astrometric standard fields might serve to calibrate the geometric distortions of many other cameras on other telescopes (including those equipped with AO, MCAO, or those space-based). However, the utility of our fields deteriorate over time since a proper motion estimate for stars in our catalogs is only provided for those stars that are in common with UCAC 4 catalog. In this paper, we make these astrometric standard fields available to the community.

<sup>2</sup> Note that this strategy had been modified for some fields. We specify these changes, when necessary, in the following subsections.

**Table 2.** List of the HAWK-I@VLT data set used for this work.

Filter	$N_{\text{dither}}$	Step (arcsec)	Exposure time (NDIT $\times$ DIT)	Image quality (arcsec)	Airmass (sec $z$ )	$\sigma$ (Radial residual) (mas)
Commissioning 1, August 3–6, 2007						
Bulge – Baade’s window (#1)						
$J$	25	95	(6 $\times$ 10 s)	0.56–1.07	1.038–1.085	4.5
$H$	25	95	(6 $\times$ 10 s)	0.40–0.76	1.081–1.149	4.3
$K_S$	25	95	(6 $\times$ 10 s)	0.25–0.45	1.042–1.091	2.8
Bulge – Baade’s window (Rotated by 135°) (#2)						
$K_S$	25	95	(6 $\times$ 10 s)	0.49–0.85	1.015–1.044	5.6
NGC 6121 (M 4)						
$J$	4 $\times$ 25	95	(6 $\times$ 10 s)	0.36–1.04	1.010–1.540	6.5
$K_S$	5	140	(6 $\times$ 10 s)	0.40–0.51	1.050–1.056	3.8
NGC 6822						
$J$	9	190	(12 $\times$ 10 s)	0.61–0.83	1.028–1.049	5.3
$K_S$	9	190	(12 $\times$ 10 s)	0.43–0.75	1.050–1.082	4.8
Commissioning 2, October 14–19, 2007						
NGC 6656 (M 22)						
$K_S$	25	47.5	(6 $\times$ 10 s)	0.28–0.41	1.252–1.420	3.1
NGC 6388						
$J$	25	95	(6 $\times$ 10 s)	0.64–0.94	1.287–1.428	9.7
$K_S$	25	95	(6 $\times$ 10 s)	0.50–0.75	1.436–1.637	12.2
JWST calibration field (LMC)						
$J$	25	95	(6 $\times$ 10 s)	0.51–0.65	1.408–1.412	5.3
$K_S$	24	95	(6 $\times$ 10 s)	0.45–0.60	1.411–1.429	4.8
Commissioning 3, November 28–30, 2007						
NGC 104 (47 Tuc)						
$J$	25	47.5	(6 $\times$ 10 s)	0.51–0.82	1.475–1.479	7.1
$K_S$	23	47.5	(6 $\times$ 10 s)	0.54–1.01	1.475–1.483	15.0

**Notes.**  $N_{\text{dither}}$  is the number of dithered images per observing block. “Step” is the dither spacing (shift in arcsec from one exposure to the next one). The integration time (DIT) times the number of individual integrations (NDIT) gives the exposure time.  $\sigma$ (Radial residual) gives an assessment of the astrometric accuracy reached (see Sect. 5.5 for the full description).

### 3.1. The Baade’s Window astrometric field

The first selected astrometric field is located in Baade’s Window. Our field is centered on coordinates  $(\alpha, \delta)_{J2000.0} \sim (18^{\text{h}}03^{\text{m}}10^{\text{s}}.4, -29^{\circ}56'48''.4)$ . Most of this field has a smooth, uniform distribution of Galactic Bulge stars. Stars just below saturation in a 60 s  $K_S$  exposure are typically separated by a few arcseconds, so that there are many of them in each field. In general, however, they are sufficiently isolated to allow us to compute accurate positions.

The choice of a cumulative integration time of 60 s was driven by two considerations. First, we wanted to have the upper main sequence in a CMD of all chosen targets to be optimally exposed with low-luminosity RGB stars still below the saturation threshold. Second, the large-scale semi-periodic and correlated atmospheric noise (with estimated scale length at  $\sim 3$ – $5'$ ) noted by Platais et al. (2002, 2006) essentially disappears at exposures exceeding 30 s. Thus, 60 s was a good compromise of integration time. According to the formula developed by Lindgren (1980) and Han (1989), a standard deviation due to atmospheric noise on the order of 15 mas is expected over the angular extent

of HAWK-I FoV. This certainly is an upper limit of the actual standard deviation because the seeing conditions of our NIR observations were 2–3 times better than those considered by the aforementioned authors for visual wavelengths.

The images were taken close to the zenith in an effort to minimize differential refraction effects, which plague ground-based images (and consequently affect the estimate of the low-order terms of the distortion solution).

The Baade’s Window field is the main field we use to derive the geometric-distortion solution that is tested for stability – or refined – with the other fields. In Sect. 5, we derive the geometric-distortion solution in this field for each of the three available filters,  $J$ ,  $H$  and  $K_S$ , using 25 images dithered with a step of about  $95''$ . In addition to this, we also collected 25  $K_S$  images of the same field but with the de-rotator at a position of  $135^\circ$  clockwise. We used this field to perform a check of the distortion with different angles (see Sect. 5.8).

In Fig. 3, we show a summary of one of these observing runs in filter  $K_S$  from left to right: the overlap of the different pointings, the stacked image, a zoom-in of the region actually used to calibrate the geometric distortion (the region highlighted

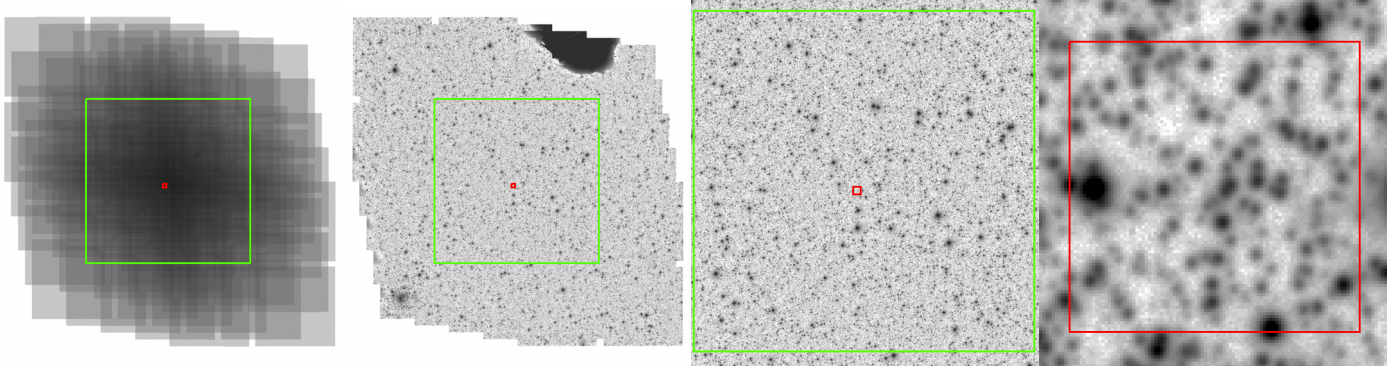


**Fig. 3.** (From left to right) *first panel:* a depth-of-coverage map of 25  $K_S$  HAWK-I’s images collected in Baade’s window during the run of August 3–6, 2007. The gray-scale goes linearly from 1 to 25. The green box is the  $7.5 \times 7.5$  patch of sky within which there are always at least five images. *Second panel:* resulting stack of the 25 images. The dark spot on the top-right is the signature left by the “shadow” of the probe, which pick-up the star used for the simultaneous Active Optic correction of the VLT/UT4’s primary mirror. On the bottom-left, there is the globular cluster NGC 6522. Note that neither the dark spot nor NGC 6522 are inside the region enclosed by the green box. *Third panel:* focuses on the green region and shows that the distribution of stars in this field is remarkably homogeneous. *Fourth panel:* zoom-in of a representative sub-set of the field (indicated by the  $10'' \times 10''$  red box in *all panels*), which is able to show a better resolved image.

in green), and a further zoom-in at a resolution able to reveal individual pixels (region indicated in red in the other panels).

### 3.2. The star-cluster astrometric fields

The tangential internal motions of Bulge stars is on average  $100 \text{ km s}^{-1}$ , and assuming an average distance of 8 kpc, this yields a proper motion dispersion of  $\sim 3 \text{ mas yr}^{-1}$  (see, for example, Bedin et al. 2003). In just a few years, proper motions this large can mask out systematic distortion trends that have amplitudes below the  $3\text{-mas-yr}^{-1}$  level (such as those discussed in Sect. 5.2). It is therefore important in some applications to have more stable astrometric fields.

For this reason, we also observed four globular clusters. Stars gravitationally bound in globular clusters have an internal velocity dispersion  $\lesssim 20 \text{ km s}^{-1}$  in their cores and are even smaller in their outskirts. Although the systemic motion of star clusters is usually different to (and larger than) the Galactic field dispersion, their common rest-frame motions are generally more than 10 times smaller than the internal motions of Bulge stars, so clusters members can be expected to serve as astrometric standards with much smaller internal proper motions.

#### 3.2.1. NGC 6656 (M 22)

The second field was centered on the globular cluster NGC 6656 (M 22). At a distance of about 3.2 kpc, M 22 ( $(\alpha, \delta)_{J2000.0} = (18^{\text{h}}36^{\text{m}}23^{\text{s}}.94, -23^{\circ}54'17''.1$ , Harris 1996, 2010 edition) is one of the closest globular clusters to the Sun.

These data were impacted by an internal reflection of the Moon in the optics, causing an abnormally-high sky value on the rightmost 300 pixels of the detector. In spite of this, the exquisite image quality of these data makes them among the best in our database. We used this field to test the solution of the geometric distortion (see Sect. 5.7 for detail).

#### 3.2.2. NGC 6121 (M 4)

The third field is centered on globular cluster NGC 6121 (M 4), ( $(\alpha, \delta)_{J2000.0} = (16^{\text{h}}23^{\text{m}}35^{\text{s}}.22, -26^{\circ}31'32''.7$ , Harris 1996, 2010 edition). It is the closest globular cluster to the Sun, and its rich star field has a small angular distance from the Galactic Bulge.

The observing strategy for the  $J$ -filter is similar to that described before. Each OB is organized in a run of 25 consecutive exposures and the same block was repeated four times in four different nights, shifting the grid by few arcsec each time.

This field was also observed in the  $K_S$ -filter but with a dither pattern completely different from the others. There are only five exposures dithered with steps of  $100''$ , which are taken with the purpose of estimating stars’ color.

#### 3.2.3. NGC 6388

NGC 6388 is a globular cluster located in the Galactic Bulge at  $(\alpha, \delta)_{J2000.0} = (17^{\text{h}}36^{\text{m}}17^{\text{s}}.23, -44^{\circ}44'07''.8$ ) (Harris 1996, 2010 edition). Some exposures of this field show the same dark spot due to the probe as in the Baade’s window (see Fig. 3).

#### 3.2.4. NGC 104 (47 Tuc)

The last globular cluster observed during the HAWK-I commissioning is NGC 104 (47 Tuc), ( $(\alpha, \delta)_{J2000.0} = (00^{\text{h}}22^{\text{m}}05^{\text{s}}.67, -72^{\circ}04'52''.6$ ) (Harris 1996, 2010 edition). Two of the 25 pointings of the  $K_S$ -filter data were not usable.

### 3.3. The extra-galactic astrometric fields

Extra-galactic fields are more stable than Galactic fields, since their internal proper motions are negligible compared to foreground stars, even with a 10-yr time baseline. The downside of such extra-galactic fields is the need to increase the integration time to compensate for the faintness of the targets.

#### 3.3.1. NGC 6822

The first extra-galactic field is centered on the Local Group dwarf irregular galaxy NGC 6822 at a distance of  $\sim 500$  kpc (Madore et al. 2009).

For this galaxy, we took fewer pointings (9 in a  $3 \times 3$  array) but with a longer integration time. Adopting the same numbers as in Fig. 2, we only used dithers labeled 1, 3, 5, 11, 13, 15, 21, 23, and 25. The integration time was 120 s with NDIT = 12 and DIT = 10 s.

### 3.3.2. An astrometric field for JWST in LMC

In 2005, a field near the center of the Large Magellanic Cloud (LMC) was selected as reference field to solve for the geometric distortion and to eventually help calibrate the relative positions of JWST's instruments in the focal plane. This field is in the JWST continuous viewing zone and it can be observed whenever necessary. In 2006, it was observed with the Advanced Camera for Surveys (ACS) Wide Field Channel (WFC) to create a reference catalog in F606W.

The field is centered at  $(\alpha, \delta)_{J2000.0} = (5^{\text{h}}21^{\text{m}}55^{\text{s}}87, -69^{\circ}29'47''.05)$ . The distortion-corrected star catalog we provide in this paper can be used as distortion-free frame to compute the geometric distortion of the JWST's detectors when the time comes. We adopted the same observing strategy as above with 25 images organized in a  $5 \times 5$  array. Unfortunately, one of the pointings in the  $K_S$ -filter data set was not usable.

## 4. PSF-modeling, fluxes and positioning

In our reductions, we used the custom-made software tools. It is essentially the same software used in the previous papers of this series. We started from a raw multi-extension FITS image. Each multi-extension FITS image stores all four chips in a datacube. We kept this FITS format up to the sky-subtraction phase.

First, we performed a standard flat-field correction<sup>3</sup> on all the images. In the master flat fields, we built a bad-pixel mask by flagging all the outliers respect to the average counts. We used the bad-pixel-mask table to flag warm/cold/dead pixels in each exposure. Cosmic rays were corrected by taking the average value of the surrounding pixels if they were not inside a star's region<sup>4</sup>; bad columns were replaced by the average between the previous and following columns.

Digital saturation in our images starts at 32 768 counts. To be safe, we adopted a saturation limit of 30 000 counts to minimize deviations from linearity close to the saturation regime (accordingly to Kissler-Patig et al. 2008) and flat-field effects. Each pixel for which the counts exceed the saturation limit was flagged and not used.

Finally, we subtracted the sky from the images, computing the median sky value in a  $10 \times 10$  grid and then subtracting the sky according to the table (bi-linear interpolation was used to compute the sky value in a given location). After the sky subtraction, we split each multi-extension FITS file in four different FITS files, one per chip. The next step was to compute the PSF models.

HAWK-I's PSF is always well sampled, even in the best-seeing condition. To compute PSF models, we developed the software `img2psf_HAWKI` in which our PSF models are completely empirical. This is derived from the WFI@2.2 m reduction package (Paper I). They are represented by an array of  $201 \times 201$  grid points, which super-sample PSF pixels by a factor of 4 with respect to the image pixels. The fraction of flux contained in the central pixel of a star is given by the central PSF pixel. A bi-cubic spline is used to interpolate the value of the PSF between the grid points. The value of a given pixel  $P_{i,j}$  in the

vicinity of a star of total flux  $z_*$  that is located at position  $(x_*, y_*)$  is:

$$P_{i,j} = z_* \cdot \psi(i - x_*, i - y_*) + s_*,$$

where  $\psi(\Delta x, \Delta y)$  is the instrumental PSF, or specifically, the fraction of light (per unit pixel area) that falls on the detector at a point offset  $(\Delta x, \Delta y) = (i - x_*, j - y_*)$  from the star's center, and  $s_*$  is the local sky background value. For each star, we have an array of pixels that we can fit to solve for the triplet of parameters:  $x_*$ ,  $y_*$ , and  $z_*$ . The local sky  $s_*$  is calculated as the  $2.5\sigma$ -clipped median of the counts in the annulus between 16 and 20 pixels from the location where the star's center falls. The previous equation can be inverted (with an estimate of the position and flux for a star) to solve for the PSF:

$$\psi(\Delta x, \Delta y) = \frac{P_{i,j} - s_*}{z_*}.$$

This equation uses each pixel in a star's image to provide an estimate of the 2-dimensional PSF at the location of that pixel,  $(\Delta x, \Delta y)$ . By combining the array of sampling from many stars, we can construct a reliable PSF model. As opposed to the pioneering work of Stetson and his DAOPHOT code (Stetson 1987) that combines an empiric and semi-analytic PSF model, we created a fully empirical PSF model, as described in Paper I.

The software `img2psf_HAWKI` iterates to improve both the PSF model and stellar parameters. The starting point is given by simple centroid positions and aperture-based fluxes. A description of the software is given in detail in Paper I.

To model the PSFs in both the core and the wings, we use only stars with a high signal-to-noise ratio (S/N). This is done by creating a list of stars that have a flux of at least 5000 counts above the local sky (i.e.,  $S/N > 60-70$  in the central pixel) and also have no brighter neighbors within 15 pixels. We need at least 50 such stars for each PSF model, so that we can iteratively reject stars that may be compromised by nearby neighbors, cosmic rays, or detector defects (e.g., bleeding columns).

Determining both a good model for the PSF and determining stellar positions and fluxes requires an iterative solution, so the software iterates this process several times until convergence is reached with both good PSF models and stellar parameters that fit well. The result is a  $5 \times 5$  grid of PSF models for each chip, which are bi-linearly interpolated to provide a model PSF at any pixel position.

With an array of PSF models, we are able to measure stars' positions and fluxes for all the stars in the image by using a software analog to that described in Paper I. As an input, we need to give the faintest level above the sky for a star to be found and determine how close this star can be to brighter neighbors. The program finds and measures all stars that fit these criteria. The final catalogs (one for each chip) contain positions, instrumental magnitudes, and another quantity called quality-of-PSF-fit (QFIT, which represents the fractional error in the PSF-model fit to the star). For each pixel of a star within the fitting radius (2.5 pixels), the QFIT is defined as the sum of the absolute value of the difference between the pixel values  $P_{i,j}$  (sky subtracted) and what the local PSF model predicts at that location  $\psi(i - x_*, j - y_*)$ , normalized with respect to the sky-subtracted  $P_{i,j}$ :

$$\text{QFIT} = \sum_{i,j} \left| \frac{(P_{i,j} - \text{sky}) - z_* \cdot \psi(i - x_*, j - y_*)}{P_{i,j} - \text{sky}} \right|,$$

where  $(x_*, y_*)$  is the star's center. The QFIT is close to zero for well-measured stars and close to unity for ones that are badly-measured (or not star-like). Typically we found  $\text{QFIT} \lesssim 0.05$

<sup>3</sup> The correction was performed using a single master flat field for each of the 3 filters. We did not use a flat field tailored to each epoch because some of them were not collected.

<sup>4</sup> Cosmic rays close to the star's center increase the apparent flux and shift the center of the star, resulting in a large QFIT value (see Appendix A for detail).

for well-measured stars in our images. Saturated stars are also measured in our pipeline. For these stars we only fitted the PSF on the wings of the stars using unsaturated pixels. In this way, we are able to measure a flux and a position for saturated stars, even if they are less accurate (high QFIT) than for unsaturated stars.

## 5. Geometric distortion correction

In this section, we present a geometric-distortion solution for the HAWK-I in three broad band filters ( $J$ ,  $H$ , and  $K_S$ ) derived using exposures of the Baade’s Window field. No astrometric reference data is available for the Baade’s Window field, so we iteratively constructed our own.

Adopting the observing strategy described in Sect. 3, the systematic errors in the measure of stars’ positions from one exposure to the other have a random amplitude and the stars’ averaged positions provide a better approximation of their true positions in the distortion-free master frame.

To build the master frame, we cross-identified the star catalogs from each individual HAWK-I chip. Conformal transformations (four-parameter linear transformations, which include rigid shifts in the two coordinates, one rotation, and one change of scale, so the shape is preserved) were used to bring the stars’ positions, as measured in each image, into the reference system of the master frame. We considered only well-measured, unsaturated objects with a stellar profile and measured in at least three different images.

Our geometric-distortion solution for HAWK-I is made up of five parts: (1) a linear transformation to put the four chips into a convenient master frame (Hereafter, we refer to the transformation from chip  $k$  of the coordinate system of image  $j$  to the master system  $T_{j,k}$ ); (2) two fifth-order polynomials to deal with the general optical distortion (hereafter, the “P” correction); (3) an analytic correction for a periodic feature along the  $x$ -axis, as related to the detector read-out amplifiers (the “S” correction); (4) a fine-tuning to correct second-order effects on the  $x$ -residuals of the S correction (the “FS” correction); and (5) a table of residuals that accounts for both chip-related anomalies and a fine-structure introduced by the filter (the “TP” correction).

The final correction is better than  $\sim 0.027$  pixel ( $\sim 2.8$  mas) in each coordinate. We provide the solution in two different forms: a FORTRAN subroutine and a set of FITS files for each filter/chip/coordinate. Since focus, flexures, and general conditions of the optics and telescope instrumentation change during the observations (within the same night and even between consecutive exposures), we derive an *average* distortion correction.

Here, we describe our correction procedure for filter  $K_S$ . The procedure for filters  $J$  and  $H$  is identical, and the results are presented in the Sect. 5.6.

### 5.1. Polynomial correction (P)

We followed the method given in Anderson & King (2003) for the Wide-Field Planetary Camera 2 (WFPC2). This method was subsequently used to derive the distortion correction for the ACS High Resolution Channel (Anderson & King 2004) and for the Wide Field Camera 3 (WFC3) Ultraviolet-Visual (UVIS) channel (Bellini & Bedin 2009; Bellini et al. 2011). The same strategy was also used by two of us to calibrate the blue prime-focus camera at the LBT (Paper IV). We treated each chip independently, and we solved the 5th-order polynomial that provided the most correction. We chose pixel (1024, 1024) in each chip

as a reference position and solved for the distortion with respect to it.

The polynomial correction is performed as follows:

- In each of the list of unsaturated stars found in each chip of each exposure ( $4 \times 25$  lists), we first selected stars with an instrumental magnitude brighter than  $K_S \simeq -11$  and with a QFIT lower than 0.05, to ensure that the master list would be free from poorly measured stars, which would harm the distortion solution.
- We computed the linear transformation ( $T_{j,k}$ ) between stars in each chip of each exposure and the current master frame.
- Each star in the master frame was conformally transformed in the raw-coordinate system of each chip/image ( $T_{j,k}^{-1}$ ) and cross-identified with the closest source. Each such cross-identification generates a pair of positional residuals ( $\delta x, \delta y$ ), which correspond to the difference between the observed position and the transformed reference-frame position.
- These positional residuals were distilled into a look-up table made up of  $12 \times 12$  elements of  $170.7 \times 170.7$  pixels each. This setup proved to be the best compromise between the need of an adequate number of grid points to model the polynomial part of the distortion solution and an adequate sampling of each grid element. We found about 19 000 pairs of residuals in each chip with a median number of 135 pairs per cell (the number varied between 30, which occurred in a corner grid element, and 170, which was near the chips’ center).
- We performed a linear least-square fit of the average positional residual of each of the 144 cells to obtain the coefficients for the two fifth-order polynomials in each chip (see Paper IV for a detailed description).
- We applied this P correction to all stars’ positions.
- Finally, we iterated the entire process, deriving a new and improved combination of a master frame and distortion solution. The residuals improved with each iteration.

The iterative process was halted when the polynomial coefficients from one iteration to the next differed by less than 0.01%.

The final P correction reduced the average distortion residuals (from the center of the detector to the corner) from  $\sim 2.1$  pixels down to  $\sim 0.2$  pixel. By applying the P correction, the accuracy of our distortion solution (defined as 68.27th percentile of the  $\sigma$ (Radial residual), see Sect. 5.5 for detail) improves from  $\sim 0.336$  to  $\sim 0.043$  pixel per coordinate for a well-exposed star, which translates from  $\sim 35.6$  mas to  $\sim 4.5$  mas. In Fig. 4, we show the HAWK-I distortion map before and after our P correction. Although the aim of our work is not to analyze what makes the distortion happen, the distortion pattern before the correction appears to be primarily a radial distortion in the focal plane with some vignetting at the edges plus some shift-rotation-shear in the detector positioning.

### 5.2. Average periodic “step” correction (S)

Our P correction reveals a high-frequency, smaller-amplitude effect, which is a periodic pattern in the  $x$ -positional residuals as a function of the  $x$  positions in all HAWK-I chips. This effect is clearly shown in the distortion map after the P correction is applied ( $\delta x$  vs.  $X$  panels in Fig. 4). For every 128 columns, stars’ positions have positive residuals (about 0.075 HAWK-I pixel) in the first 64 pixels and negative residuals (about 0.045 HAWK-I pixel) in the second 64 pixels (see panels (a) of Fig. 5). At first glance, this residual pattern has the appearance of being caused

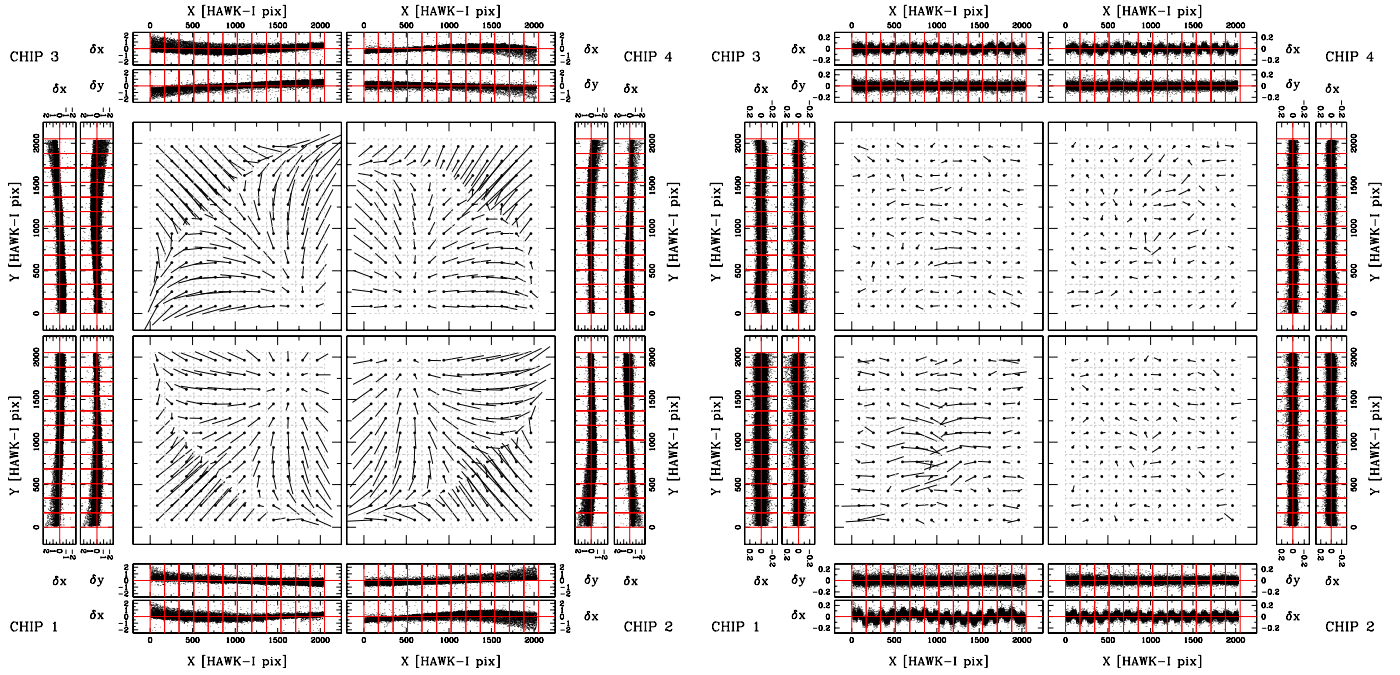


**Fig. 4.** HAWK-I@VLT distortion map for  $K_s$  filter. *Left*: residual trends for the four chips when we use uncorrected stars' positions. The size of the residual vectors is magnified by a factor of 500. For each chip, we also plot the single residual trends along X and Y axes. Units are expressed in HAWK-I raw pixel. *Right*: residuals after our polynomial correction is applied. The size of the residual vectors is now magnified by a factor 5000.

by irregularities in the pixel grid of the detectors. However, a detailed analysis (see Sect. 6) leads us to conclude that it is instead a pattern caused by a “periodic lag” in the readout process, which is offset in opposite directions in alternating 64 pixel sections of the detector addressed by each of the 32 read-out amplifiers.

We adopted an iterative procedure to empirically correct for this periodic pattern that shows up only along the x axis. We started with the master frame made by using catalogs corrected with our P correction. We then transformed the position of each star ( $i$ ) from the master frame back into the raw coordinate system of each chip ( $k$ ) of each image ( $j$ ). We determined the quantity:

$$\delta x_i = x_i^{\text{raw}} - x_{i,j}^{P^{-1}(T_{jk}^{-1})},$$

where  $x_i^{\text{raw}}$  are the raw  $x$ -coordinates, and  $x_{i,j}^{P^{-1}(T_{jk}^{-1})}$  are the  $x$ -coordinates on the master frame transformed to the raw coordinate system and corrected with the inverse P correction. We assumed that the periodic trend had a constant amplitude across the detector. Panels (a) in Fig. 5 show  $\delta x$  vs.  $x^{\text{raw}}$  for each chip (from 1 to 4) and  $\delta x$  vs.  $x^{\text{raw}}$  modulus 128, in which we collect together all the residuals (panel 5) before applying the S correction.

To model the trend in the residuals, we used a square-wave function (panel (5-a) of Fig. 5). The amplitude of this function is defined as the  $3\sigma$ -clipped median value of the residuals between pixels 2.8–62.2 and 66.8–126.2. To model the average periodicity between  $62.2 \leq x^{\text{raw}} \leq 66.8$  pixels, we fitted the data points with a straight line using linear least squares.

We corrected the stars' positions by applying 75% of the S correction (to encourage smooth convergence) and the P correction. We computed an improved master frame and calculated new, generally smaller, residuals. New square-wave-function amplitudes were derived and added to the previous corrections to improve the S correction. The procedure was iterated until the

observed average periodicity residuals had an amplitude smaller than  $10^{-4}$  pixel.

Combining the two corrections (S+P, applied in this order to the raw coordinates), we are able to reduce the 68.27th percentile of the  $\sigma(\text{Radial residual})$  down to  $\sim 4.0$  mas (0.038 pixel).

### 5.3. Fine-tuned correction of the residual periodicity (FS)

In panels (b) of Fig. 5, we show the residual trend after the S + P correction is applied. Looking at panels (1–4b), it is obvious that the amplitude of the  $\delta x$  periodicity pattern is not constant from chip to chip. In addition to this, there is still a polynomial residual that needs to be removed. For this reason, we applied a fine-tuned residual correction as follows.

We first computed a master frame by applying the S + P correction to the raw positions of each chip/exposure. We then determined the residuals as the difference between the raw  $x$ -coordinates corrected with the S correction and  $x_{i,j}^{P^{-1}(T_{jk}^{-1})}$ . Next, we divided each chip into 32 bins of 64 pixels each along the  $x$  axis, computed the  $3\sigma$ -clipped average value of the residuals, and subtracted the 75% of it from the  $\delta x$  residuals in each bin. Then, we iterated the procedure until the difference between the  $3\sigma$ -clipped average value of the residuals in all bins of all chips from one iteration to the next one was smaller than  $10^{-3}$  pixel. In panels (c-1) to (c-4) of Fig. 5, we show the residual trends for all chips after our S + FS + P corrections are applied.

This approach was able to provide accuracies (68.27th percentile of the  $\sigma(\text{Radial residual})$ ) down to 0.035 pixel ( $\sim 3.7$  mas) level.

### 5.4. Table of residual geometric-distortion correction (TP)

The final step of our distortion-solution model consists of four look-up tables (one for each chip) to minimize all the remaining

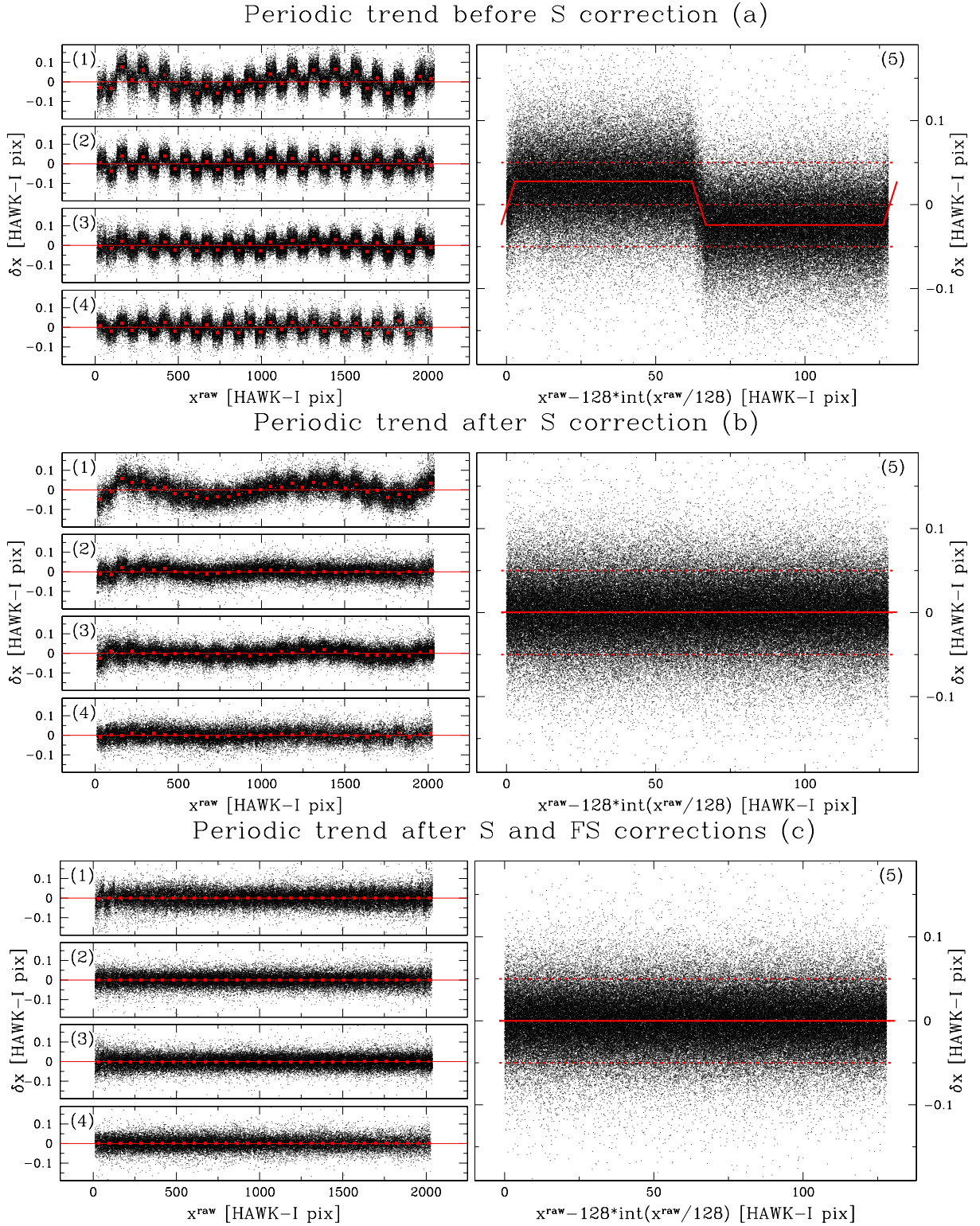


**Fig. 5.** *Top:*  $\delta x$  as a function of  $X$  in units of HAWK-I pixels before S correction. *Middle:* as above but after S correction. *Bottom:* same as above but after S and FS corrections. In the *left panels* (from 1 to 4), we took 32 bins of 64 pixels each and computed the median of residuals in each bin (red squares). In the *right panels* (5), we show the periodogram with a period of 128 columns containing all the points plotted in the *left panels*. The dashed red lines show  $+0.05$ ,  $0$ , and  $-0.05$  HAWK-I pixel.

detectable systematic residuals that were left. We constrained the look-up tables using the same procedure that Bellini, Anderson & Bedin (2011) used to derive the distortion correction for the WFC3/UVIS camera.

First, we corrected all stars' positions by applying the S, FS, and P corrections (in this order). We then built a new master frame and computed the residuals, as described in Sect. 5.1. We subdivided again each chip into  $12 \times 12$  square elements. We used

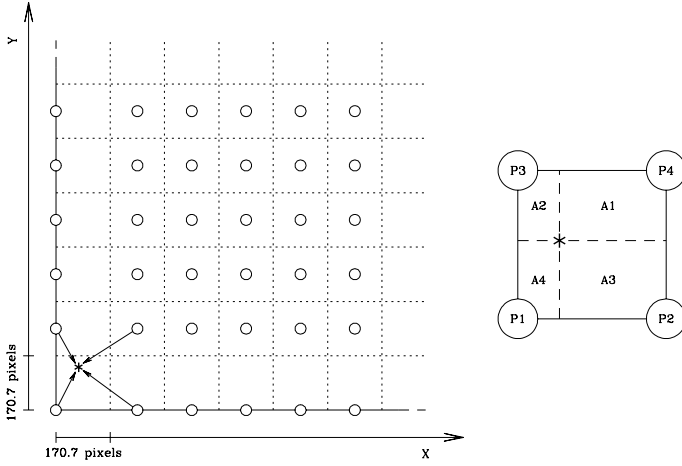


**Fig. 6.** *Left:* example of cell and grid-point locations on the bottom-left area of chip[1]. Dotted lines mark the  $170.7 \times 170.7$  pixels square elements inside which we computed the median value of the distortion residual to use as grid point (empty circles) in the look-up table. For a given star (marked with an \*), we used the four surrounding closest grid point to perform the bi-linear interpolation (sketched with the arrows) and evaluate the residual geometric distortion in that location of the detector. *Right:* Bi-linear interpolation outline. Each grid point  $P_1, \dots, P_4$  is weighted by the corresponding area  $A_1, \dots, A_4$  to associate the correction in \*.

the stars' residuals within each cell to compute a  $3\sigma$ -clipped median positional residuals and assigned these values to the corresponding grid points (open circles in Fig. 6). When a cell adjoins detector edges, the grid point is displaced to the edge of the cell, as shown. For the grid point on the edges, the value of the median only at the first iteration is computed at the center and shifted to the edge. Then, we iteratively found the value that the grid-point element on the edge should have to remove the systematic errors. We built a look-up table correction for any given location of the chip, using a bi-linear interpolation among the surrounding four grid points. Figure 6 shows an example of the geometry adopted for the look-up table and of the bi-linear interpolation.

We corrected stars' positions using only 75% of the recommended grid-point values, computed an improved master frame, and calculated new (generally smaller) residuals. We calculated new grid-point values and added them to the previous values. The procedure was iterated until the bi-linear interpolation offered negligible improvement of the positional residuals rms from one iteration to the next.

### 5.5. Accuracy of the geometric-distortion correction

In Fig. 7, we show the final HAWK-I distortion map after we applied our full distortion solution (S + FS + TP + P). To have a reliable assessment of the errors in the distortion correction, we computed the rms of the position residuals of each star ( $i$ ) observed in each chip ( $k$ ) of the image ( $j$ ), which have been distortion corrected and conformally transformed into the master-frame reference system  $(x_{i,j,k}^{T,jk}, y_{i,j,k}^{T,jk})$ . The difference between these positions and the distortion-free positions  $(X_i^{\text{master}}, Y_i^{\text{master}})$

directly quantifies how close we are to reach the ideal distortion-free system. We defined the  $\sigma$ (Radial residual) as:

$$\sigma(\text{Radial residual})_{i,j} = \sqrt{\frac{(x_{i,j,k}^{T,jk} - X_i^{\text{master}})^2 + (y_{i,j,k}^{T,jk} - Y_i^{\text{master}})^2}{2}}$$

In Fig. 8, we show the size of these  $\sigma$ (Radial residual) versus instrumental  $K_S$  magnitude after each step of our solution. To test the accuracy of the geometric-distortion solution, we only used unsaturated stars with an instrumental magnitude  $K_S \leq -12.4$  (dashed red line) in the master list, which is observed in at least 3 images and with a QFIT  $\leq 0.05$ . Faint stars have larger residuals due to an increasing contribution of random errors. The  $3\sigma$ -clipped 68.27th-percentile value of these residuals is shown on the right of each panel. The  $3\sigma$  clipping rule excludes outliers, which can bias the percentile value. These outliers can have different explanations. For example, most of the outliers for the Bulge field are close to the edge of the FoV, where the distortion solution is less constrained. In the case of NGC 6656, most of these outliers are close to the center of the cluster (crowding effects) or are located in the region affected by the internal reflection of the Moon in the optics. Hereafter, we refer in the text with  $\sigma_{\text{perc}}$  to the  $3\sigma$ -clipped 68.27th-percentile value of the  $\sigma$ (Radial residual). The distributions of the rms is very non-Gaussian and the 68.27th-percentile is an arbitrary choice to represent the errors. Although it is not absolutely correct mathematically, it gives a good indications of where an outlier will lie.

In the bottom panel, we plot the  $\sigma$ (Radial residual) obtained using more-general 6-parameter linear transformations to compute the master-frame average positions. These transformations also include other two terms that represent the deviation from the orthogonality between the two axes and the change of relative scale between the two axes (the shape is not preserved anymore). When general linear transformations are applied, most of the residuals introduced by variations in the telescope+optics system and differential atmospheric refraction are removed, and  $\sigma_{\text{perc}}$  further reduces to 0.027 pixel ( $\sim 2.8$  mas).

### 5.6. Geometric-distortion correction for J and H filters

Each HAWK-I filter constitutes a different optical element, which could slightly change the optical path and introduce changes in the distortion. To test the filter-dependency of our  $K_S$ -based distortion solution, we corrected the positions measured on each  $J$ - and  $H$ -filter images of Baade's Window field with our  $K_S$ -filter-derived distortion solution and studied the residuals. We found  $\sigma$ (Radial residual) significantly larger than those obtained for the  $K_S$ -band images. We also tried to apply the  $K_S$ -filter distortion solution plus an ad-hoc table of residual (TP correction) for each filter without significant improvements. For these reasons, we decided to independently solve for the distortion for the  $J$  and  $H$  images.

We built the  $J$ -filter master frame using only stars with an instrumental magnitude brighter than  $J \simeq -11.5$  and with a QFIT  $\leq 0.05$ . For the  $H$ -filter, we built the master frame using only stars with  $H \simeq -12.5$  and, again, QFIT  $\leq 0.05$ . We adopted these selection criteria to sample each chip with an adequate number of stars (at least 12 000 and 19 000 stars for the  $J$ - and  $H$ -filter, respectively). The distortion corrections were performed as described in the previous sections.

As shown in Table 2, the image quality of the  $J$ -filter Bulge images changed dramatically during the night of the observation,

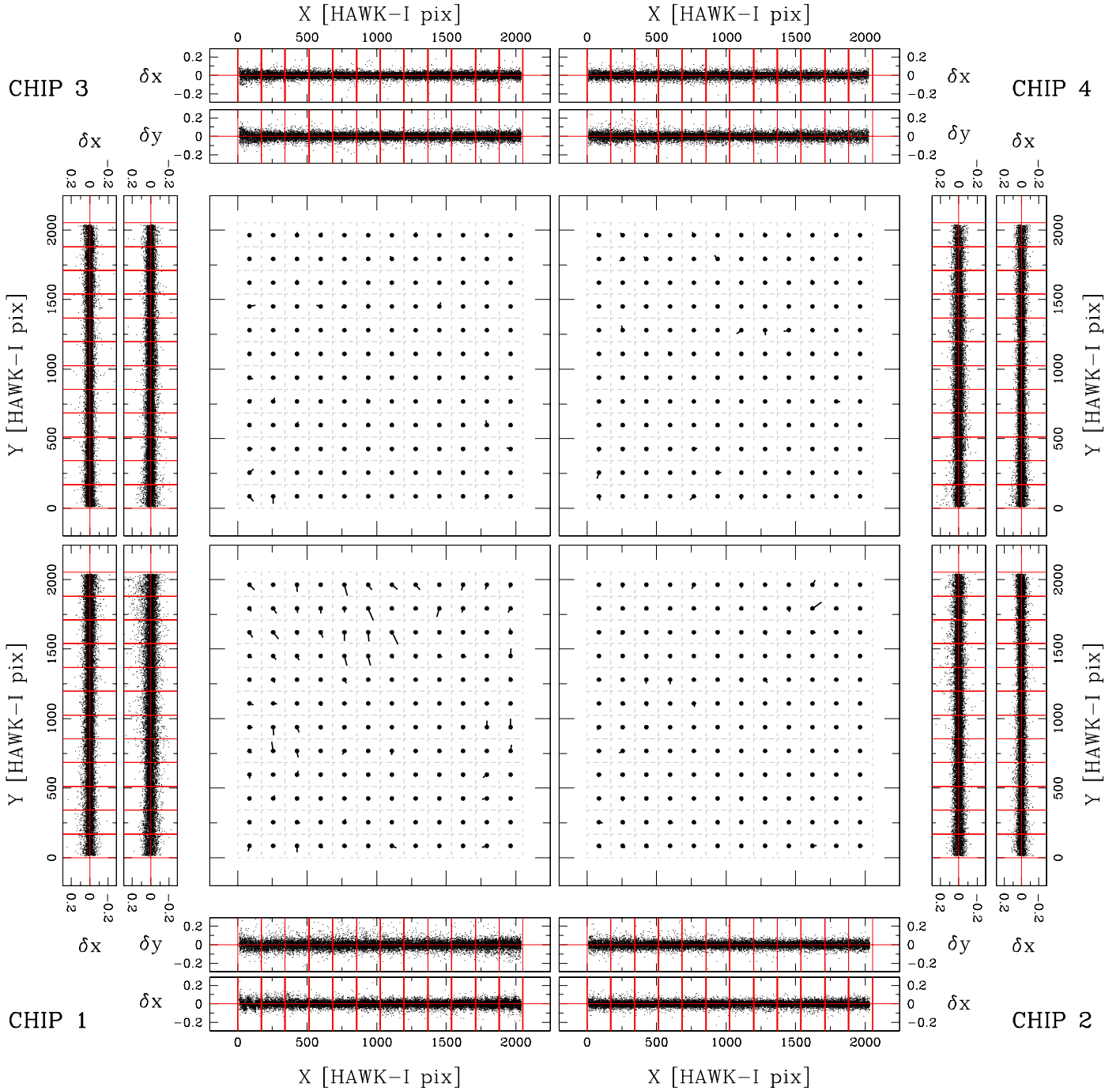


**Fig. 7.** As Fig. 4 but after we have applied all the distortion corrections. The size of the residual vectors are now magnified by a factor 10 000.

reaching 1.07 arcsec. We initially used all *J*-filter images to compute the distortion correction and obtained a  $\sigma_{\text{perc}}$  (using general transformations) of  $\sim 6.8$  mas. We then only considered those exposures with an image quality better than  $FWHM = 0.80$  arcsec and re-derived the distortion correction (57 out of 100 catalogs were excluded this way).

In Fig. 9, we show that the  $\sigma(\text{Radial residual})$  before and after applying the distortion correction for the *J* and *H* images. The  $\sigma_{\text{perc}}$  for well-measured unsaturated stars is shown on the right of each panel. Using general linear transformations, we obtained  $\sigma(\text{Radial residual})$  of  $\sim 4.5$  mas and  $\sim 4.3$  mas for *J* and *H* filter, respectively.

On the left panel in Fig. 10, we compare the residual trends obtained by applying the  $K_S$ -filter correction to *J*-filter Bulge images (blue vectors) to the residual trends obtained by applying the *J*-filter correction instead (red vectors). In the right panel, we show the same comparison for the *H*-filter case. A clear residual trend (up to 0.1 pixel) is present when a correction made for a different filter is applied to a given data set of images. The optical system performances are different at different wavelengths, so it is not surprising that the  $K_S$  solution is not completely suitable for the *J*- and *H*-filter data. The filter also introduces an additional optical element that leads to a different distortion on the focal plane. Both  $\sigma(\text{Radial residual})$  and distortion maps tell

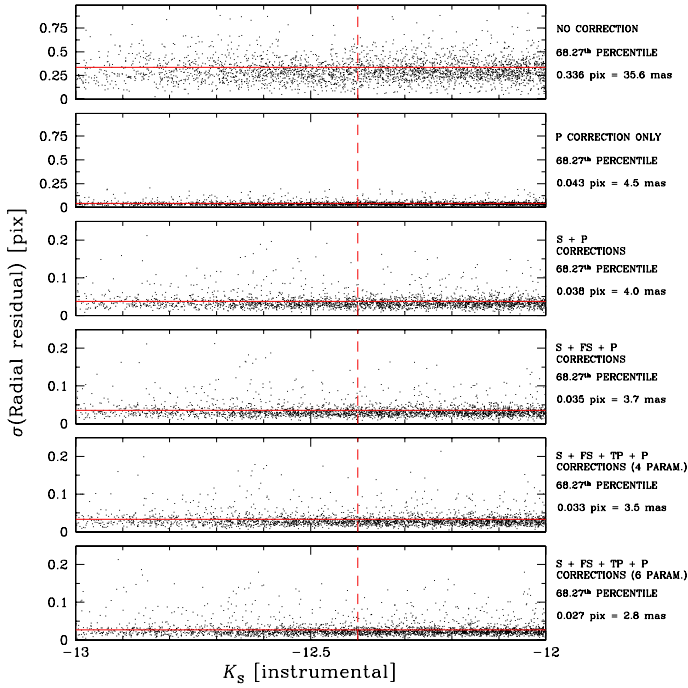


**Fig. 8.**  $\sigma(\text{Radial residual})$  versus instrumental  $K_S$  magnitude after each step of our solution. The horizontal solid red line shows the  $\sigma_{\text{perc}}$ ; the vertical dashed red line indicates the magnitude cut-off  $K_S = -12.4$ .

us that an auto-calibration for the distortion correction in each filter is required for high-precision astrometry.

### 5.7. Stability of the correction

Different factors (e.g., the contribution given by light-path deviations caused by filters, alignment errors of the detector on the focal plane) change the HAWK-I distortion over time. To explore the stability of our derived distortion solution over time, we observed the astrometric precision obtained by applying our distortion correction to images taken several months apart.

We applied our distortion solution to images of NGC 6656 (M 22) taken during the second commissioning. The  $\sigma_{\text{perc}}$  (computed as described in Sect. 5.5) was found to be  $\sim 3.5$  mas for well-measured unsaturated stars. To estimate the stability of the distortion correction over the 3-month time baseline between the first and second commissioning, we derived an independent distortion solution from the second commissioning run images and compared the results. We adopted the same auto-calibration method described above. In this way, we were able to reduce the 1D rms down to  $\sim 3.1$  mas. In Fig. 11, we show the comparison between the  $\sigma(\text{Radial residual})$  after we applied the Bulge-based distortion correction (bottom) and the newly made NGC 6656-based correction (top). The difference between these distortion solutions is only 0.003 pixel. Therefore, our Bulge distortion correction should be stable at a 3-mas level on a 3-month scale for general uses. In Fig. 12, we show the distortion-map comparison. There are systematic trends when the  $K_S$ -filter Bulge solution is applied to this data set. Nevertheless, for high-precision astrometry, we suggest auto-calibrating the distortion correction for each data set, as it is continuously evolving.

We note that the positions of the nodes of the periodic trend did not change over this trim baseline, adding support to our conclusion that this periodic residual is linked to the *detector's*

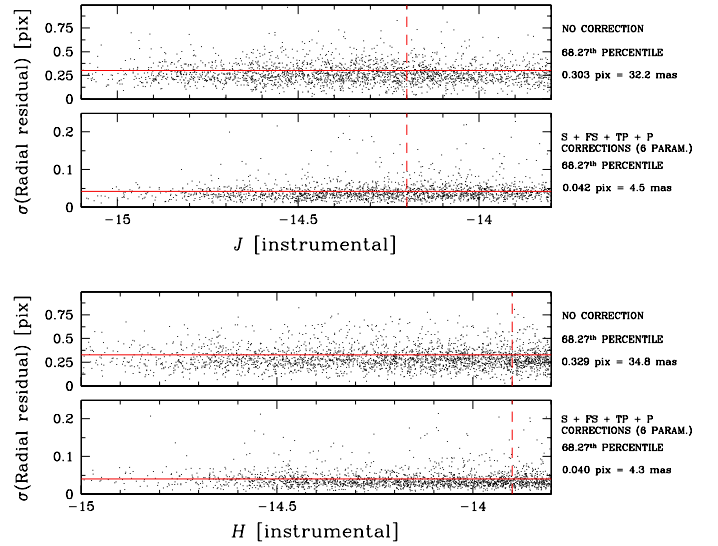


**Fig. 9.** In each half of the figure, we show the  $\sigma(\text{Radial residual})$  vs. instrumental magnitude before and after we applied our distortion correction for the  $J$  (Top) and  $H$  (Bottom). The red lines have the same meaning as in Fig. 8 but the vertical dashed red lines are set at  $J = -14.2$  (top) and  $H = -13.9$  (bottom), respectively.

properties and is not a function of the telescope, epoch, filter, or image quality (see Sect. 6).

### 5.8. An external check

As done in the previous section for the case of NGC 6656, we apply the distortion correction obtained by self-calibration of Bulge images (hereafter, Bulge#1) to a different data set, which is collected for the same field, but with the de-rotator at a different position angle at  $\sim 135^\circ$  (hereafter, Bulge#2). In this case, we obtained a  $\sigma_{\text{perc}}$  of  $\sim 5.8$  mas, which is significantly larger than that obtained in Sect. 5.5 for Bulge#1 ( $\sigma_{\text{perc}} \sim 2.8$  mas). This may give the impression that the distortion solution obtained for Bulge#1 is not suitable for the rotated images of Bulge#2. However, self-calibration of these rotated images gives us a  $\sigma_{\text{perc}}$  of  $\sim 5.6$  mas, indicating only a marginal improvement. The lower accuracy of the distortion solution of Bulge#2 must be ascribed to the intrinsic lower quality of this data set (worse average seeing, higher airmass, worse weather conditions, guiding, and instrument+telescope conditions). The distortion maps obtained applying the two solutions to the same data set (Fig. 13) highlight different trends (even if the residuals are lower than 0.05 pixel), in the upper-right corner of chip[4], which recommends again the auto-calibration for the distortion solution of each data set for high-accuracy astrometry.

Nevertheless, even if rotated Bulge#2 images were taken under worse conditions, the value of their  $\sigma_{\text{perc}} \sim 5.6$  mas allows us to make an important external check of our solution down to this level. The astrometric quantity  $\sigma_{\text{perc}}$  tells us how accurately we can expect to register the *relative* position of a star among different dithered images. However, these are internal estimates of the error, and do not account for all of the sources of systematic errors. For a better estimate of the uncertainty on the relative position of stars, we compared the two calibrated master frames of Bulge#1 and Bulge#2 and measured how much the two frames deviate from each other. We know the linear terms could be different due to change in the thermal- or flexure-induced focal

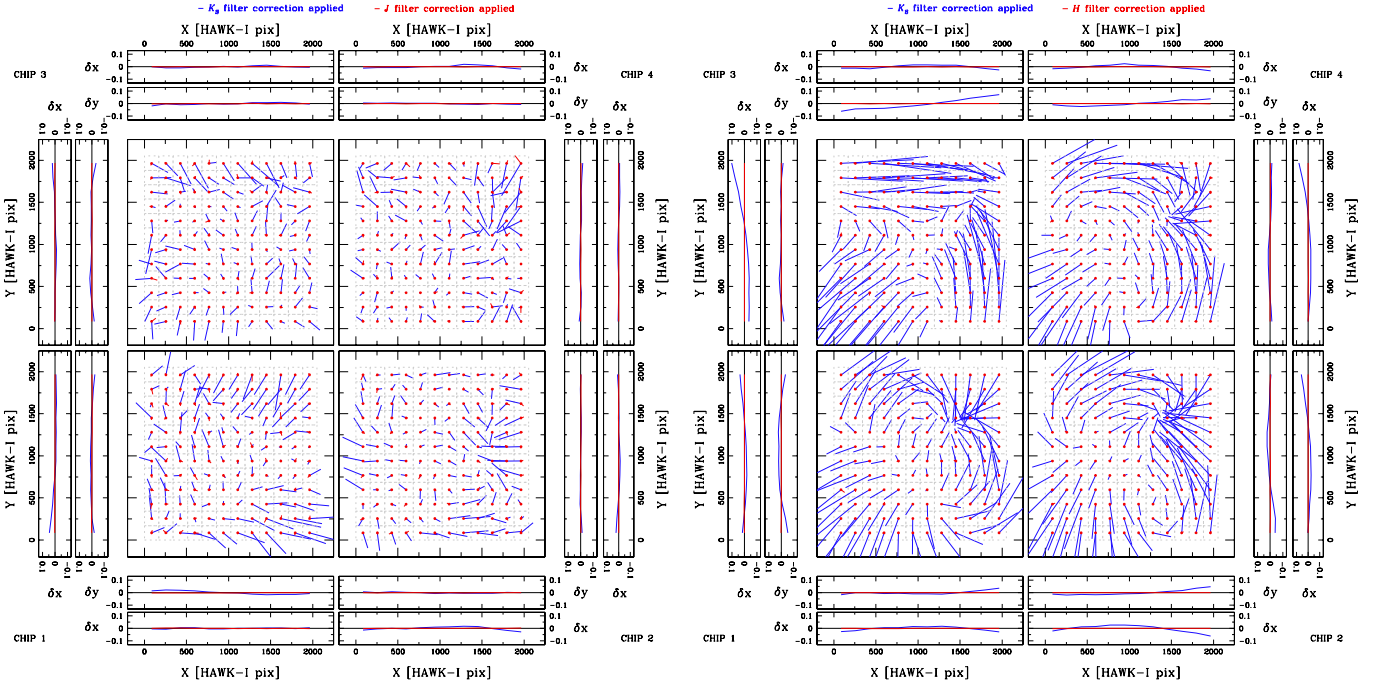


**Fig. 10.** *Left:*  $J$ -filter distortion map comparison. In blue, we plot the vectors when the  $K_S$ -filter correction is applied; in red, we show when the  $J$ -filter correction is used. We plot the single residual trends along  $X$  and  $Y$  axes with the same colors, but we do not plot the single stars to not create confusion in the plot. *Right:* the same but for the  $H$  filter. The size of the residual vectors is magnified by a factor 6000 in both panels.

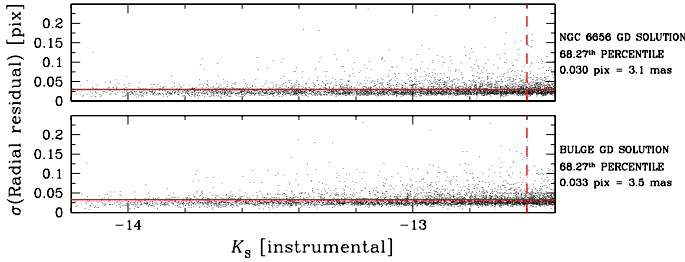


**Fig. 11.** Comparison of NGC 6656  $\sigma(\text{Radial residual})$  after application of the Bulge-based (*bottom*) and the NGC 6656-based (*top*) correction. The horizontal solid red line shows the  $3\sigma$ -clipped value of the  $\sigma(\text{Radial residual})$ ; the vertical dashed red line indicates the magnitude limit  $K_S = -12.6$ .

lengths, differential atmospheric refractions, etc. For this reason, we transformed the two master frames of Bulge#1 and Bulge#2 using general linear transformations and measured the amount of residuals in the non-linear part of the distortion. For this test, we only used those regions of both master frames where stars were measured in at least 10 images (out of 25). In Fig. 14, we show the residual trend of bright, unsaturated stars between the 2 frames. The 68.27th percentile of the  $\Delta X$  distribution is about 10.7 mas, while that of  $\Delta Y$  is about 9.4 mas. Thus, the non-linear terms of our distortion solution can be transferred between observing runs at the 10 mas level.

### 5.9. Description of the geometric-distortion-correction subroutines released

We release FORTRAN routines to correct the geometric distortion, using the solution computed for the Bulge#1 field (Sects. 5.1, 5.2, 5.3 and 5.4). There are three different routines

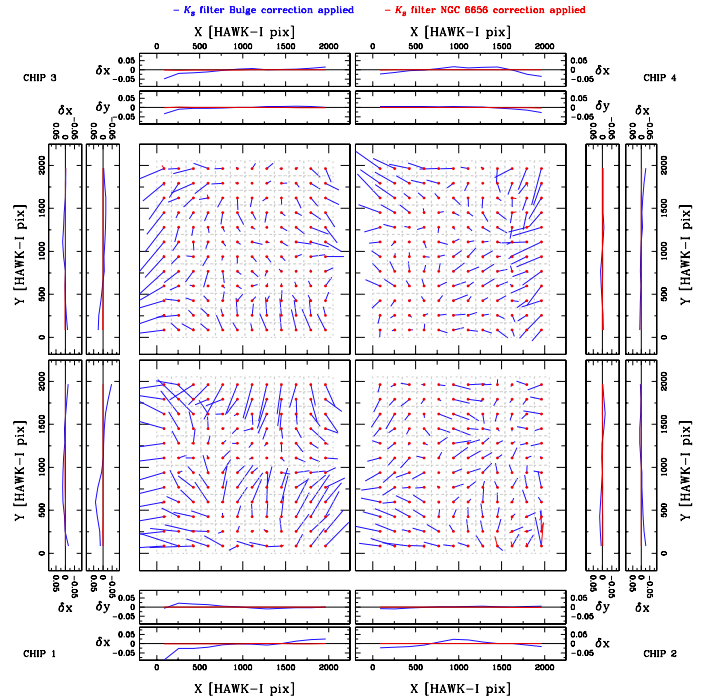


**Fig. 12.** As in Fig. 10 but for the NGC 6656 case. In blue, we plot the vectors when the Bulge correction is applied, and in red, we show when the NGC 6656-made solution is applied. The size of the residual vectors is magnified by a factor 6000.

with one for each filter ( $J$ ,  $H$ ,  $K_S$ ). They require  $x^{\text{raw}}$  and  $y^{\text{raw}}$  coordinates and the chip number. In output, the codes produce  $x^{\text{corr}}$  and  $y^{\text{corr}}$  corrected coordinates. Both raw and corrected coordinates are in the single-chip reference frame ( $1 \leq x^{\text{raw}}, y^{\text{raw}} \leq 2048$ ). In addition to these codes, we

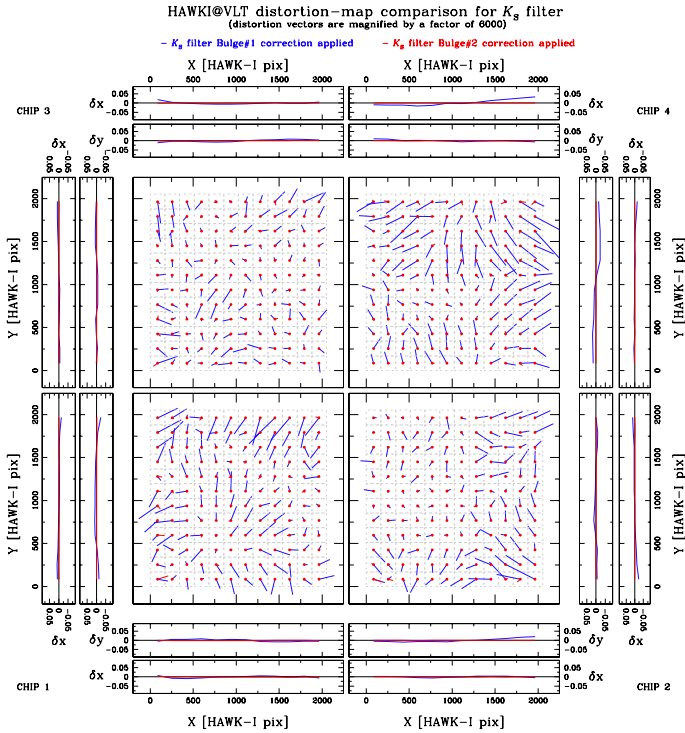


**Fig. 13.** As in Fig. 10 but for the Bulge#2 case.

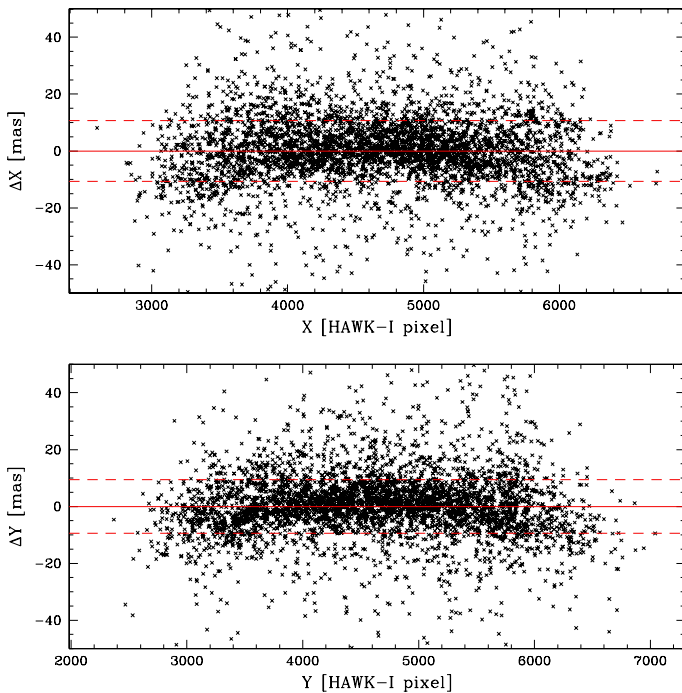


**Fig. 14.** *Top:*  $\Delta X$  vs.  $X$  between the two Bulge fields. We plotted only bright unsaturated stars. *Bottom:* as *top* panel but with  $\Delta Y$  vs.  $Y$ . The solid red line is set at 0 mas, while the dashed lines are set at  $\pm 10.7$  mas in the *top* and  $\pm 9.4$  mas in the *bottom* panel.

release our distortion solution as FITS images (one per each coordinate/chip/filter) to make the distortion solutions also available for other program languages. Bi-linear interpolation must be used to compute the amount of the distortion correction in inter-pixel locations. We refer to Appendix B for a brief description of these corrections. Furthermore, we release FITS images (one per chip/filter) that could be used to correct the

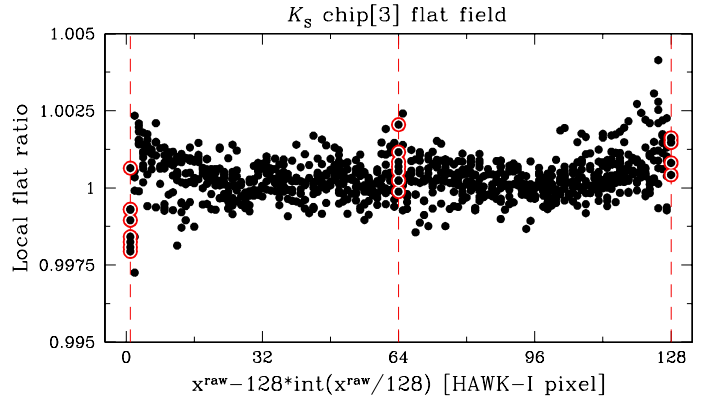


**Fig. 15.** Local flat ratio of  $K_S$  chip[3] flat field. Dashed red lines mark the boundaries of the possible discontinuities. There are not significant local flat ratio variations at the 1st, 64th, and 128th columns (highlighted by red open circles).

variation in the pixel area across the FoV. These images are useful for improving the HAWK-I photometry.

## 6. A possible explanation of the periodicity

In Sect. 5.2, we have corrected for the periodic trend observed in the  $\delta x$  positions. At first, this component might suggest the presence of some irregularities in the pixel grid, due to manufacturing defects, such as an imperfect alignment in the placement of the lithographic stencils that established the pixel boundaries on the detector. Examples include, the well-known 34th-row error found by Anderson & King (1999) in the case of the CCDs of the WFPC2 of the *Hubble* Space Telescope (HST), or, for a more recent example, the pattern observed on the detectors of the HST's WFC3/UVIS channel (see Bellini et al. 2011, for details). If the square wave that we see here in the HAWK-I  $\delta x$  residuals (from a-1 to a-4 panels of Fig. 5) is due to a geometric effect, then the variation in pixel spacing would cause periodic features in the flat fields, since wider pixels collect more light when the detector is illuminated by a flat surface brightness. In this case, the observed  $\delta x$ -residual trend would imply that the 64th and the 65th pixels in each row would be physically smaller than the 128th and the 129th pixels.

To verify this hypothesis, we computed the local flat ratio as described in Bellini et al. (2011). We took the ratio of the pixel values over the median of the 32-pixel values on either side along  $X$  direction (independently for each of the amplifiers). We computed the median value of this ratio for all pixels within  $400 < y^{\text{raw}} < 1900$  in each column. We did this for each column between  $100 < x^{\text{raw}} < 1900$  pixels. We chose this particular area to avoid some artefacts in the flat field near the edge of each chip. We then plotted the local flat ratio as a function of the 128-column pattern. The plot for chip[3] of the  $K_S$ -filter flat field is shown in Fig. 15 as example. The variation of the flat ratio of all chips in the vicinity of the Cols. 1, 64, and 128 is lower than 0.25%, thus suggesting an uniform pixel grid.

Another possible explanation of this effect can be ascribed to the readout process of the Rockwell detectors. The Rockwell HgCdTe detectors are designed to have three output modes. It can use 1, 4 or 32 amplifiers. The HAWK-I detector is set up to use all 32 amplifiers, and it takes 1.3 s to read out the entire chip. In the 32-amp mode, the chip is divided into thirty-two 64-pixel-wide strips, each fed into a different amplifier. The adopted

operating mode performs the read-out from left-to-right in even amplifiers and from right-to-left in odd amplifiers.

An apparent shift of the stars' position along the  $x$  axis may happen if there is a “periodic lag” during the read out, since the amplifier reads the pixels in sequence. This effect is very similar to the “bias shift” observed in ACS/WFC of the HST after part of the electronics, in particular the new amplifiers, has been replaced during service mission 4 (Golimowski et al. 2012). As for ACS, the readout electronics of HAWK-I's detectors take a while to settle to a new value when the charge of another pixel is loaded. Without waiting an infinite amount of time to settle down, there is some imprint left from the previous pixel. Although HAWK-I's NIR-detectors are very different from the ACS/WFC CCDs, a similar effect, or, an inertia of discharging the capacitors to reset to a new value, could cause the observed periodicity. Furthermore, each amplifier in the 32-amp mode reads 64 pixels, and 64 pixels is the observed periodicity of the effect that we found. This suggests that the cause of the periodic trend we see in the distortion could be related to the amplifiers' setup.

## 7. Weeding out spurious objects

We applied our Bulge-based distortion correction, derived as in Sect. 5, to the entire data set with the exceptions of the Bulge#2 and NGC 6656 fields, where we applied the distortion correction computed from their own exposures. We also produced stacked images to have a visible reference for our catalogs.

While analyzing the catalogs and inspecting the stacked images, we noted the presence of some faint, spurious objects identified as stars and close to brighter stars. Many of these objects were found to be in fact PSF artefacts and are not real stars. These artefacts are called “PSF bumps”. These bumps can easily mimic faint, real stars in the proximity of much brighter stars. Normally, PSF bumps are located at the same radial distance from the PSF center and have about the same brightness level. Because of these two characteristics, PSF bumps can be removed. Therefore, we introduced a flag to purge the catalogs from these detections. This flag may necessary exclude a few real stars, but faint stars close to a bright one could not be well measured anyway.

To flag these spurious objects, we followed the same approach as described in Sect. 6.1 of Anderson et al. (2008). We first selected all stars fainter than a specific instrumental magnitude (e.g. for 47 Tuc, shown in Fig. 16, we chose  $J \geq -10$ ) and with a QFIT  $\geq 0.4$ . For each of such objects, we computed the magnitude difference and the distance from the closest bright star (e.g.  $J \leq -11$  for the case of 47 Tuc) out to 15 pixels. We then plotted those magnitude differences as a function of the radial distance (top panel of Fig. 16). Different clumps show up on the plot. We drew-by-hand a region around them that encloses most of these spurious objects (in red). In this way, we built a mask (one for each filter/field) used to purge PSF artefacts.

The selection we made is a compromise between missing faint objects near bright stars and including artefacts in the catalog. In the bottom panel of Fig. 16, the red circles show all the detected objects in the 47 Tuc catalog. In the bottom right panel of Fig. 16, the green circles highlights the objects that have been finally accepted as real stars. The bright star close to the bottom of the figure has a faint neighbor (pointed by the arrow) that clearly is not an artefact but has been unfortunately flagged-out by our mask. These flagged stars represent only a very small fraction with respect to the total number of PSF artefacts removed by our procedure.

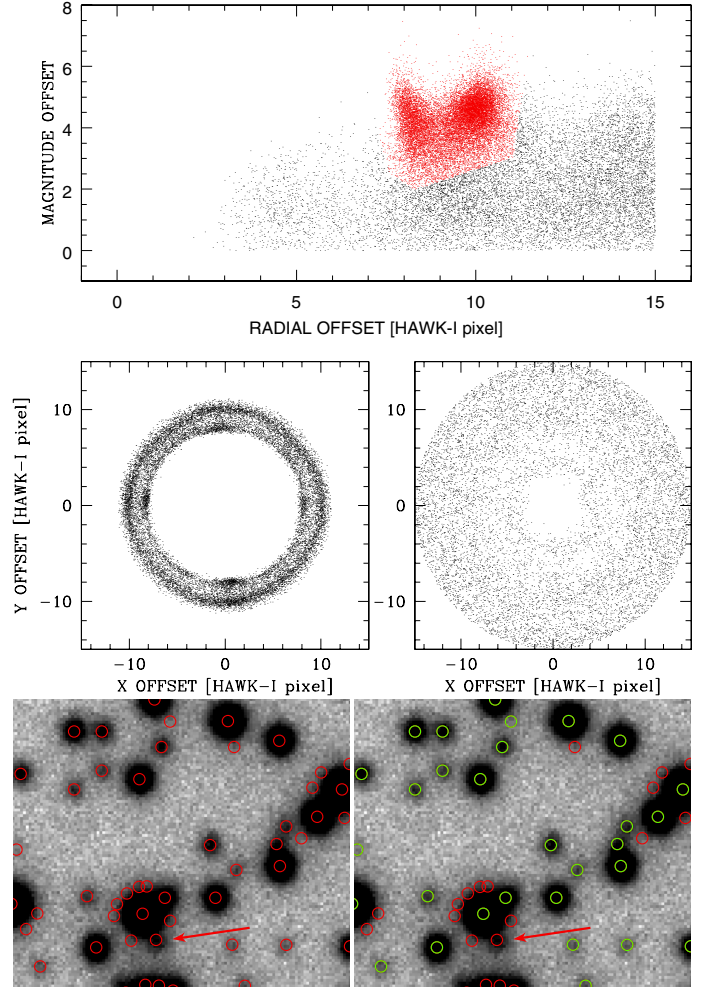


**Fig. 16.** Example of the weeding process for the 47 Tuc catalog. *Top:* magnitude offset versus radial offset for sources found around bright stars. We plotted the spurious objects that have been rejected in red. *Middle:*  $Y$  vs.  $X$  separation of the rejected (*left*) and accepted (*right*) detections from the corresponding bright stars. *Bottom:* on the *left*, we show all the objects (red circles) in a  $\sim 100 \times 100$  pixels region in the 47 Tuc catalog, and on the *right*, we highlight the detections that have been accepted (green circles). As described in the text, a faint star near the bright one pointed by the red arrow on the bottom has been flagged even if it was not an artefact.

In each final catalog, we added a column for each filter called  $F_{\text{weed}}$ . The flag  $F_{\text{weed}}$  is equal to 0 for those objects rejected by our mask. The only exception is the  $K_S$ -filter catalog of Bulge#1, for which the purging was not possible because of the too-high number of objects in the catalog that did not allow us to build a reliable mask for the PSF artefacts.

## 8. Photometric calibration

In this section, we provide two calibrations of the zero-points. The first calibration was performed using the 2MASS photometric system (Skrutskie et al. 2006) and the second calibration using the native system of the HAWK-I filters.

**Table 3.** List of the HAWK-I filter zero-points, rms, number of stars used, and zero-point formal uncertain ( $\sigma/\sqrt{N-1}$ ) to which 2MASS error of the stars used to calibrate should be added in quadrature.

Field	Filter	2MASS				MKO			
		Zero-point	$\sigma$	$N$	$\sigma/\sqrt{N-1}$	Zero-point	$\sigma$	$N$	$\sigma/\sqrt{N-1}$
Bulge – Baade’s window (#1)	<i>J</i>	-28.31	0.07	995	0.01	-28.25	0.07	966	0.01
	<i>H</i>	-28.60	0.05	57	0.01	-28.57	0.05	37	0.01
	<i>K<sub>S</sub></i>	-28.01	0.09	543	0.01	-27.98	0.09	543	0.01
Bulge – Baade’s window (#2)	<i>K<sub>S</sub></i>	-27.77	0.09	543	0.01	-27.75	0.09	542	0.01
NGC 6121 (M 4)	<i>J</i>	-28.76	0.06	298	0.01	-28.71	0.06	298	0.01
	<i>K<sub>S</sub></i>	-28.69	0.09	86	0.01	-28.67	0.09	86	0.01
NGC 6822	<i>J</i>	-28.40	0.04	28	0.01	-28.36	0.04	28	0.01
	<i>K<sub>S</sub></i>	-27.59	0.07	26	0.01	-27.57	0.07	26	0.01
NGC 6656 (M 22)	<i>K<sub>S</sub></i>	-27.95	0.15	83	0.02	-27.93	0.15	81	0.02
NGC 6388	<i>J</i>	-28.46	0.06	289	0.01	-28.41	0.06	286	0.01
	<i>K<sub>S</sub></i>	-27.73	0.05	229	0.01	-27.72	0.05	229	0.01
JWST calibration field (LMC)	<i>J</i>	-28.78	0.07	233	0.01	-28.74	0.07	226	0.01
	<i>K<sub>S</sub></i>	-27.84	0.09	122	0.01	-27.82	0.09	123	0.01
NGC 104 (47 Tuc)	<i>J</i>	-28.26	0.05	80	0.01	-28.22	0.05	80	0.01
	<i>K<sub>S</sub></i>	-27.71	0.05	128	0.01	-27.69	0.05	128	0.01

**Notes.** The values listed in columns (3) to (6) are those obtained in the 2MASS system, and from (7) to (10) in the MKO system.

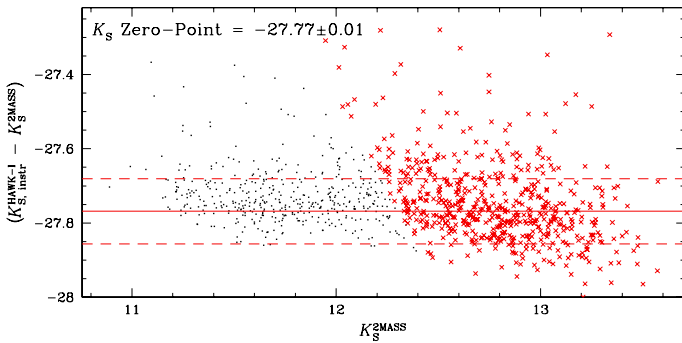


**Fig. 17.** Magnitude difference between HAWK-I and 2MASS as function of the 2MASS magnitude. The black dots represent all the stars matched between HAWK-I and 2MASS with good photometry. Red crosses show stars from the saturation limit ( $K_S = -15.46$ ) to two magnitudes fainter. The solid red line is the zero-point (median of the magnitude difference of the red crosses); the dashed line are set at a zero-point  $\pm 1\sigma$  (defined as the 68.27th percentile of the distribution around the median). The label in the top left corner gives the zero-point  $\pm \sigma/\sqrt{N-1}$ , where  $N$  is the number of stars used to compute the zero-point.

### 8.1. 2MASS system

The first photometric calibration was performed using the 2MASS catalog. Since 2MASS is a shallow survey, we only got a small overlap between unsaturated stars in HAWK-I images and 2MASS data covering a very narrow magnitude range near the faint limit of 2MASS. Therefore, we can apply a single zero-point calibration only. We selected well-measured bright unsaturated stars within two magnitudes from saturation in our catalogs to calculate these photometric zero-points. In Fig. 17, we show the case of the Bulge#2 catalog, as an example. For the Bulge#1

*K<sub>S</sub>*-filter, we first registered the zero-point to that of the Bulge#2, and then used the Bulge#2 zero-point due the low number of unsaturated stars in common with 2MASS.

In Table 3, we list the zero-points, their rms ( $\sigma$ ), the number of stars used to compute the zero-points ( $N$ ) and  $\sigma/\sqrt{N-1}$  (formal error values) for all fields. These are estimates of the zero-point uncertainties and not the errors because the 2MASS errors are not added in quadrature. Note that we only provide one zero-point for each filter/field and not one for each chip/filter/field. We registered all chips in the flat-fielding phase to the common reference system of chip[1], and while building the master frame, we iteratively registered the zero-point of all chips to that of the chip[1].

As clearly visible in Fig. 17, this calibration is not perfect, but there is a more conceptual limitation of this calibration. The filters of HAWK-I are in the Mauna Kea Observatory (hereafter, MKO) photometric system, which have pass-bands slightly different from the 2MASS pass-bands and are likely to contain a color term.

### 8.2. MKO system

As suggested by the Referee, determining the zero-points in the native MKO photometric system would be a more rigorous zero-point calibration.

Therefore, we transformed the 2MASS magnitudes into the MKO system using the transformations described in the 2MASS Second Incremental Release website<sup>5</sup> for 2MASS stars

<sup>5</sup> [http://www.ipac.caltech.edu/2mass/releases/allsky/doc/sec6\\_4b.html](http://www.ipac.caltech.edu/2mass/releases/allsky/doc/sec6_4b.html)

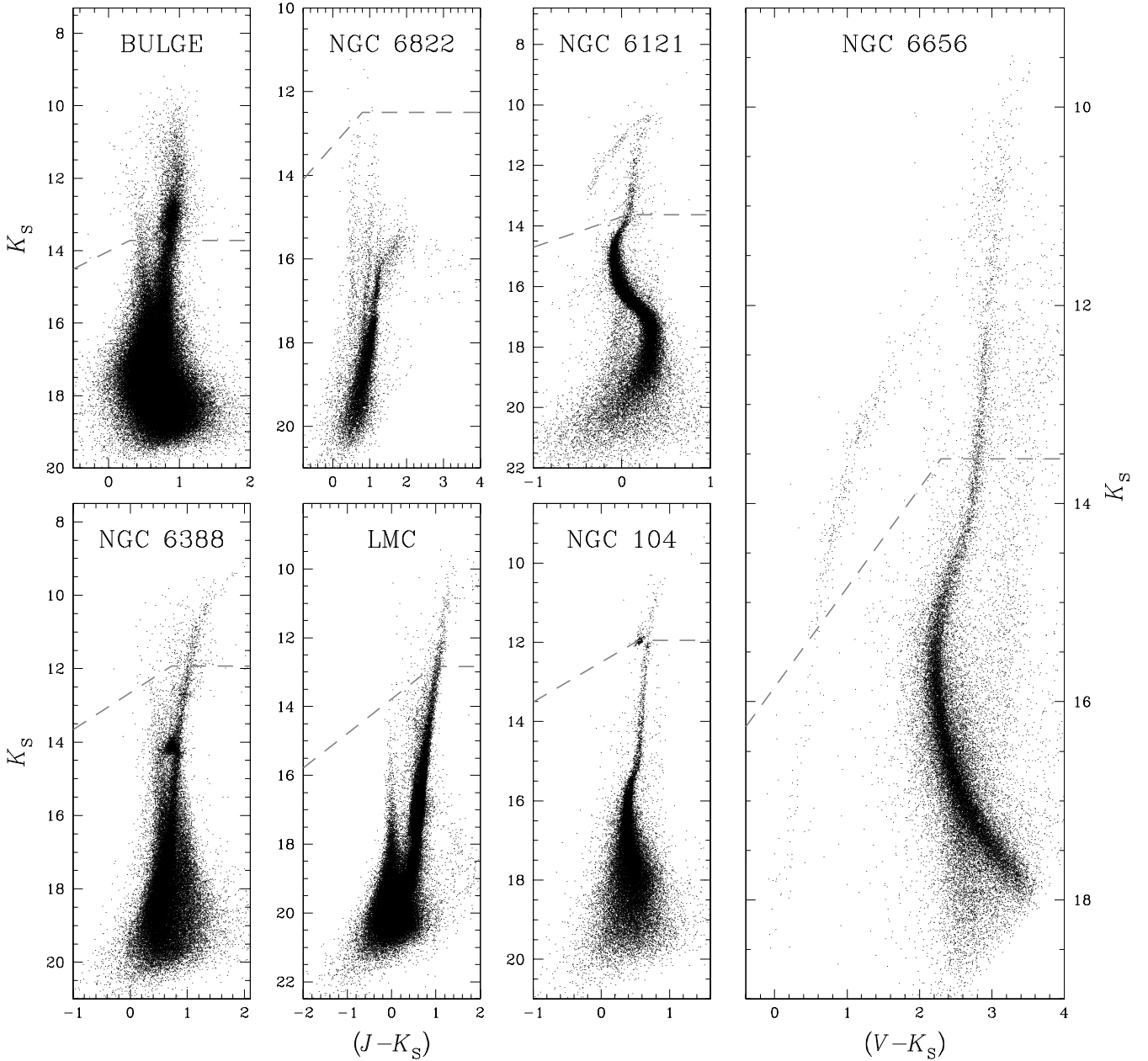


**Fig. 18.** Full set of CMDs of the fields used in this paper. The dotted gray lines set the saturation threshold in  $K_S$  filter.

in common with our catalogs:

$$\begin{aligned}
(K_S)_{2\text{MASS}} &= (K)_{\text{MKO}} + (0.002 \pm 0.004) \\
&\quad + (0.026 \pm 0.006)(J - K)_{\text{MKO}}, \\
(J - H)_{2\text{MASS}} &= (1.156 \pm 0.015)(J - H)_{\text{MKO}} + (-0.038 \pm 0.006), \\
(J - K_S)_{2\text{MASS}} &= (1.037 \pm 0.009)(J - K)_{\text{MKO}} + (-0.001 \pm 0.006), \\
(H - K_S)_{2\text{MASS}} &= (0.869 \pm 0.021)(H - K)_{\text{MKO}} + (0.016 \pm 0.005).
\end{aligned}$$

We used only 2MASS stars that, once transformed in the MKO system, were in the color range  $-0.2 < (J - K)_{\text{MKO}} < 1.2$ . We then registered the zero-points as described in the previous section. We found an average difference between the MKO and 2MASS zero-points of 0.05, 0.03, and 0.02 mag in  $J$ -,  $H$ -, and  $K_S$ -filter, respectively. For the  $K_S$  filter in NGC 6121 catalog, we did not have enough stars to compute the zero-point in the color range in which the transformations are valid, so we added the

average  $K_S$ -filter offset (0.02 mag) between the two systems to the 2MASS-based zero-point. In Table 3, we also list the MKO zero-points (with their  $\sigma$ ,  $N$ , and  $\sigma/\sqrt{N-1}$ ).

## 9. Applications: NGC 6656 and NGC 6121

Figure 18 shows a full set of CMDs with one for each field. For the HAWK-I data used in this section, the photometric zero-points are those obtained in the 2MASS system (Sect. 8.1). We chose two possible targets among the observed fields to illustrate what can be done with HAWK-I. The two close globular clusters NGC 6656 and NGC 6121 have high proper motions relative to the Galactic field. In the ESO archive, we found WFI@2.2 m MPI/ESO exposures of the same fields taken  $\sim 8$  years before our HAWK-I observations. These exposures allow us to obtain

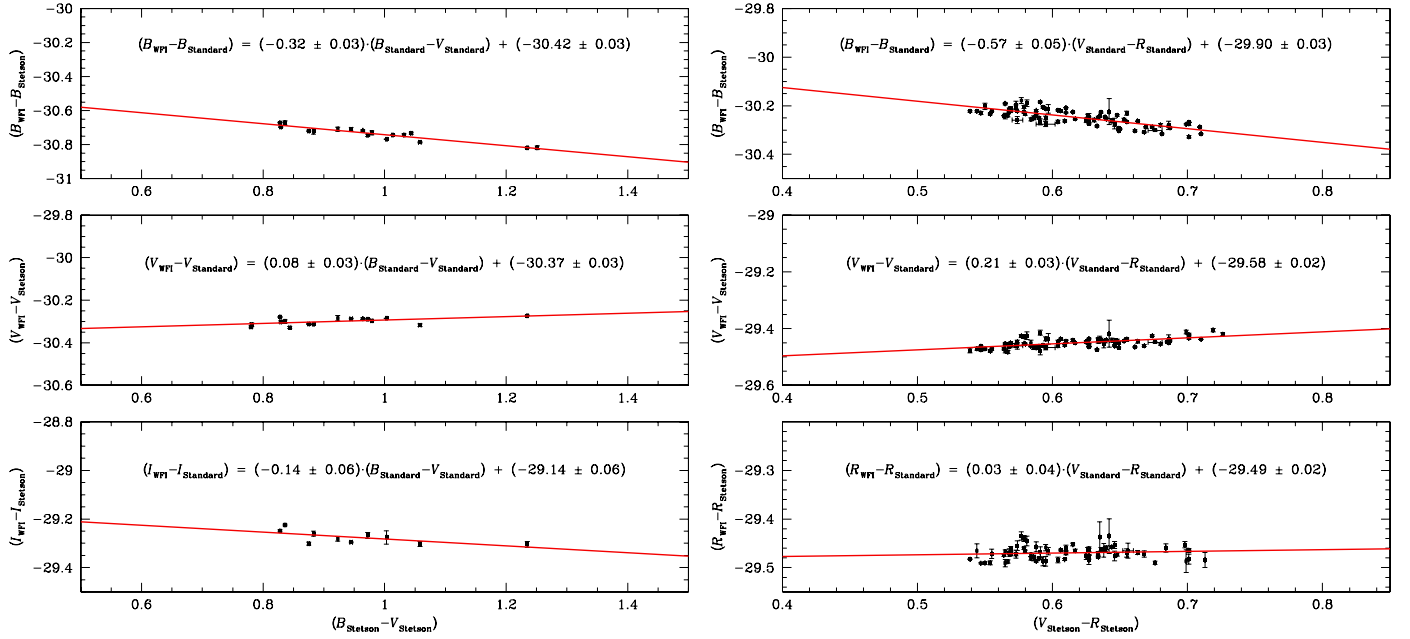


**Fig. 19.** *Left:* calibration fits and equations for  $B$ ,  $V$ , and  $I$  filters for NGC 6656. *Right:* same as on the left but for  $B$ ,  $V$ , and  $Rc$  filters for NGC 6121.

a nearly-perfect separation between cluster and field stars, as we will show in the following subsections.

### 9.1. WFI data set: photometric calibration and differential reddening correction

We downloaded multi-epoch images of NGC 6656 from the ESO archive (data set 163.O-0741(C), PI: Renzini), taken between May 13 and 15 1999 in  $B$ ,  $V$ , and  $I$  filters with the WFI@2.2 m MPI/ESO. These images were not taken for astrometric purposes and only have small dithers, thus preventing us from randomizing the distortion-error residuals. Photometry and astrometry were extracted with the procedures and codes described in Paper I. Photometric measurements also were corrected for sky concentration effects (light contamination caused by internal reflections of light in the optics, causing a redistribution of light in the focal plane) using recipes in Paper III. The WFI photometry was calibrated matching our catalogs with the online secondary-standard stars catalog of Stetson (Stetson 2000, 2005) using well-measured, bright stars, and least-square fitting. We found that a linear relation between our instrumental magnitudes and Stetson standard magnitudes was adequate to register our photometry. The calibration equations are shown in Fig. 19 in the left panels.

As for NGC 6656, we downloaded the NGC 6121 images from the ESO archive taken with the WFI@2.2 m MPI/ESO between August 16 and 18 1999, in  $B$ ,  $V$ , and  $Rc$  filters. We performed the photometric calibration as described above. The corresponding calibration fit and equations are shown in Fig. 19 in the right panels.

In the following subsections, we explore some applications in which the photometry has been corrected for differential reddening. We performed a differential reddening correction following the iterative procedure described in Milone et al. (2012). As described in detail by Milone et al., the correction to apply to a given star is measured from the differential reddening of the selected reference stars that are spatially close to the target. The

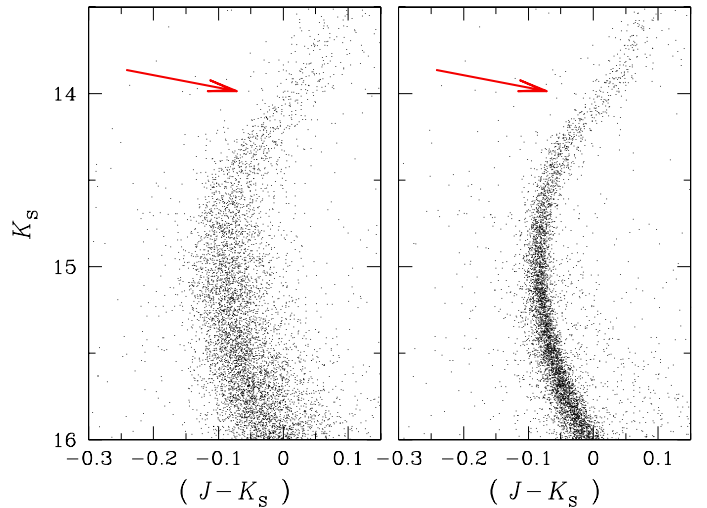


**Fig. 20.** Zoom-in of the  $K_S$  vs.  $(J - K_S)$  CMD of NGC 6121. We show the CMDs before and after the differential reddening correction is applied (*left* and *right* panels respectively). The red arrow indicates the reddening direction.

number of stars to use should be a compromise between the need to have an adequate number of reference stars to compute the correction and the need for spatial resolution. We chose the nearest 45 reference stars from the faint part of the red giant branch (RGB) to the brighter part of the main sequence (MS) to compute the correction. In Fig. 20, we present an example to demonstrate how the CMDs change by taking the differential reddening into account and correcting for it. We show a zoom-in of the NGC 6121  $K_S$  vs.  $(J - K_S)$  CMD before (left panel) and after (right panel) the correction. Around the MS turn-off ( $K_S \sim 15$ ), the sequence narrowed from  $\Delta(J - K_S) \sim 0.08$  to  $\sim 0.03$  mag. Hereafter, all CMDs for both NGC 6656 and NGC 6121 are corrected for differential reddening.

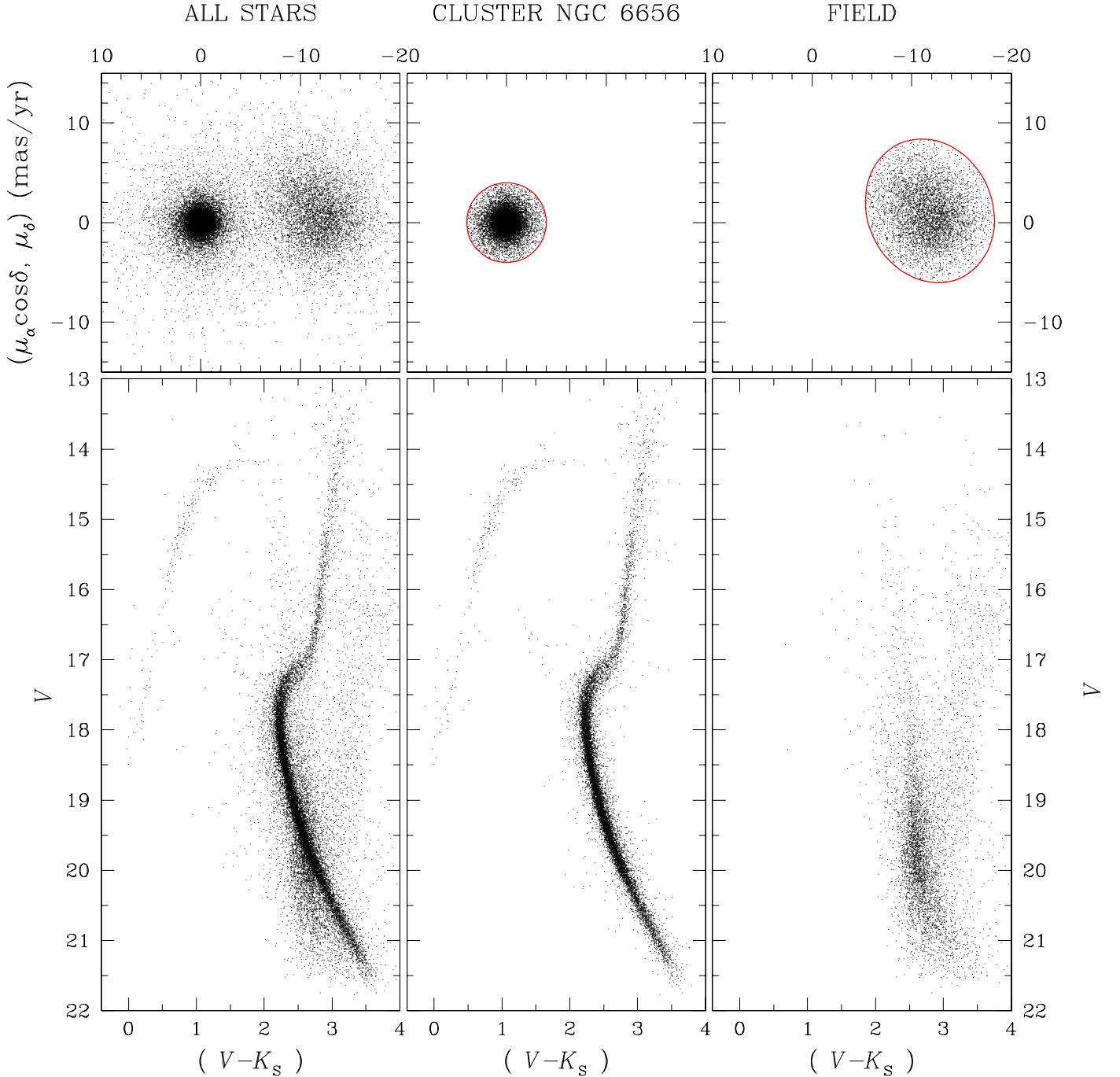


**Fig. 21.** *Top panels:* proper motion vector–point diagram with a  $\sim 8$ -yr time baseline between HAWK-I and WFI data. The  $(0, 0)$  location in VPD is the mean motion of cluster stars candidates. *Bottom panels:*  $V$  vs.  $(V - K_S)$  color–magnitude diagram. *Left:* the entire sample. *Center:* stars in VPD with proper motion within  $4 \text{ mas yr}^{-1}$  around the cluster mean. *Right:* probable background/foreground field stars in the area of NGC 6656 studied in this paper. The ellipse that encloses most of the field stars is centered at  $(-11.8, 1.2) \text{ mas yr}^{-1}$  with major and minor axes of  $12.5$  and  $14.8 \text{ mas yr}^{-1}$ , respectively.

## 9.2. NGC 6656 proper motion

To compute proper motions, we followed the method described in Paper I, to which we refer for the detailed description of the procedure. For the WFI images, we only used those chips that overlap with the HAWK-I field and with an exposure time of  $\sim 239 \text{ s}$  for a total of 19 first-epoch catalogs that include  $B$ ,  $V$ , and  $I$  filters. With the 100 catalogs for the second epoch (HAWK-I) in  $K_S$  band, we computed the displacements for each star. As described in Paper I, the local transformations used to

transform the star’s position in the 1st epoch system into that of the 2nd epoch minimize the effects of the residual geometric distortion.

In Fig. 21, we show our derived proper motions for NGC 6656. We show only stars with well-measured proper motions. In the left panels of Fig. 21, we show the entire sample of stars; the middle panels display likely cluster members. The right panels show predominantly field stars. In the middle vector-point diagram (VPD), we drew a circle around the cluster’s

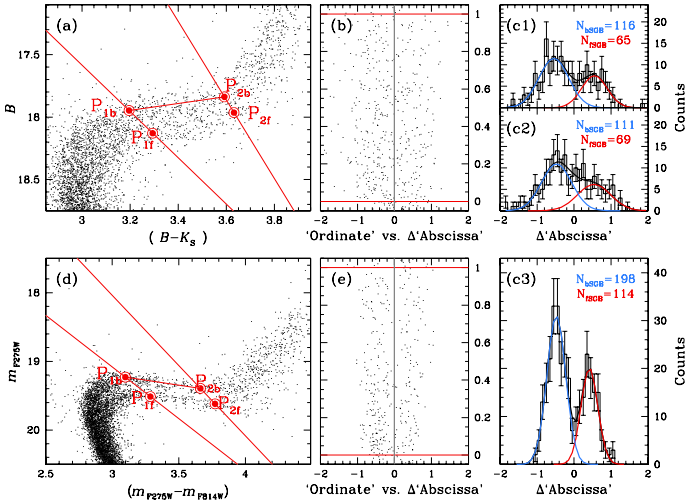


**Fig. 22.** **a)** SGB zoom-in on  $B$  vs.  $(B - K_S)$  CMD of NGC 6656. The four points (and the two straight lines) used to perform the linear transformation are plotted in red. **b)** Rectified SGB. The red horizontal lines are set at “Ordinate” 0 and 1; the gray solid line is set at  $\Delta$ “Abscissa” = 0. **c1)** Dual-Gaussian fit in black; individual Gaussian in blue and red are used for bright and faint SGB respectively, for the SGB-star sample between 1.5 and 3.0 arcmin from the cluster center. **c2)** As for **c1)** but in the range 3.0–9.0 arcmin. **c3), e), d)** Same as in panels **a), b), c1), c2)** but for the HST data in the  $m_{F275W}$  vs.  $(m_{F275W} - m_{F814W})$  plane.

motion centroid of radius  $4 \text{ mas yr}^{-1}$  to select proper-motion-based cluster members. The chosen radius is a compromise between missing cluster members with larger proper motions and including field stars that have velocities equal to the cluster’s mean proper motion. This example demonstrates the ability of our astrometric techniques to separate field and cluster stars. To enclose most of the field stars, we drew an ellipse centered at  $(-11.8, 1.2) \text{ mas yr}^{-1}$  in the right VPD with major and minor axes of  $12.5$  and  $14.8 \text{ mas yr}^{-1}$ , respectively.

We analyzed the impact of the differential chromatic effects in our astrometry for this cluster as done in Anderson et al. (2006). Using unsaturated stars and with a color baseline of about 3 mag, the effects seem to be negligible (less than 1 mas/yr in each direction) within the airmass range of our data set. Thus we assumed to be negligible and did not correct it.

### 9.2.1. The radial distribution of NGC 6656 SGB stars

The sub-giant branch (SGB) based on HAWK-I data remains broadened even after the differential reddening correction. This is not surprising since NGC 6656 is known to have a split SGB (Piotto et al. 2012). The large FoV of our data set allowed us to study the behavior of the radial trend of the ratio  $\hat{p}_{fSGB} = N_{fSGB}/(N_{fSGB} + N_{bSGB})$ , where  $N_{bSGB}$  and  $N_{fSGB}$  are the number of stars belonging to the bright (bSGB) and the faint SGB (fSGB), respectively. First of all, we computed this ratio for SGB stars between 1.5 and 3.0 arcmin from the center of the cluster (we adopted the center given by Harris 1996, 2010 edition), and between 3.0 and 9.0 arcmin (close to the edge of the FoV). We chose these two radial bins to have about the same number of SGB stars in both samples. Since the innermost region (within 1.5 from the center) of the cluster is too crowded to be analyzed with the HAWK-I data, we also used the data set of Piotto et al. (2012) to have a third, inner point.

To compute the  $N_{fSGB}/(N_{fSGB} + N_{bSGB})$  ratio, we rectified the SGBs using an approach similar to that described in Milone et al. (2009). In this analysis, we used only cluster members with good photometry. The results are shown in Fig. 22. We started by using HAWK-I data only. As described by Milone et al., we need four points (P1b, P1f, P2b, and P2f in Fig. 22) to rectify the SGBs. Once selected these points, we transformed the CMD into a new reference system in which the points P1b, P1f, P2b, and P2f have coordinates (0, 0), (1, 0), (0, 1), and (1, 1), respectively. We drew by hand a line to separate the two sequences. We derived a fiducial line for each SGB by dividing it into bins of 0.12 “Ordinate” value and fitting the  $3.5\sigma$ -clipped median “Abscissa” and “Ordinate” for each of them with a spline. We rectified the two sequences using the average of the two fiducials. The rectification was performed by subtracting, from the “Abscissa” of each star, the “Abscissa” of the fiducial line at the same “Ordinate” level (panel (b)). In panels (c1) and (c2), we show the resulting final  $\Delta$ “Abscissa” histogram (between  $\Delta$ “Abscissa”  $-0.19$  and  $+0.19$  and “Ordinate” 0 and 1) for stars between 1.5 and 3.0 arcmin (c1) and between 3.0 and 9.0 arcmin (c2) from the cluster center. The individual Gaussians for the bright and the faint SGB are shown in blue and red, where the sum of the two in black. After this complicated procedure, we were finally able to estimate the fraction of stars belonging to the fSGB and bSGB. We used binomial statistics to estimate the error  $\sigma$  associated with the fraction of stars. We defined  $\sigma_{\hat{p}_{fSGB}} = \sqrt{\hat{p}_{fSGB}(1 - \hat{p}_{fSGB})/(N_{fSGB} + N_{bSGB})}$ .

As noted by Piotto et al. (2012), points P1b-P2b and P1f-P2f define a mass interval for stars in the two SGB segments. If we want to calculate the absolute value of the ratio  $\hat{p}_{fSGB}$ , we need to make sure that the same mass interval is selected in the two SGBs and at all radial distances. Due to the lack of appropriate isochrones for the HAWK-I data, this was not feasible. Still, we can estimate the radial trend of  $\hat{p}_{fSGB}$  by taking advantage of both HST (for the inner region) and HAWK-I (for the outer region) data by making sure that we use the same mass interval for the bSGB (and the same mass interval for the fSGB) in both data sets.

For this reason, we cross-correlated our HAWK-I catalog with that of Piotto et al. (2012). First, we selected the sample of SGBs stars in the  $B$  vs.  $(B - K_S)$  CMD between the P1b, P1f, P2b, and P2f points of panel (a) in Fig. 22. In the  $m_{F275W}$  vs.  $(m_{F275W} - m_{F814W})$  CMD, we selected the same stars. In this CMD, we fixed four points that enclose these stars, used them to rectify the SGBs, and then calculated the ratio by following the same procedure as described for HAWK-I data (panels (c3), (d), and (e) in Fig. 22). We emphasize that these intervals are not the same as the ones used in Piotto et al. (2012), but we used approximately (within the uncertainties due to difficulty to select the limiting points) the same mass intervals in calculating the three SGB population ratios.

The trend of the  $\hat{p}_{fSGB}$  ratio is shown in Fig. 23. To give a more reliable estimate of the error bars, we also included the histogram binning uncertainty (We computed the ratio varying the starting point/bin width in the histogram and estimate the  $\sigma$  of these values.) and quadratically added them to  $\sigma_{\hat{p}_{fSGB}}$ . In any case, these error bars still represent an underestimate of the total error because other sources of uncertainty should be taken in account (e.g., the uncertainty in the location of the limiting points of the selected SGB segments). The error bars are larger for the two HAWK-I points because of the smaller number of objects in the sample.

Our conclusion is that the radial trend of the two SGB populations within the error bars is flat.

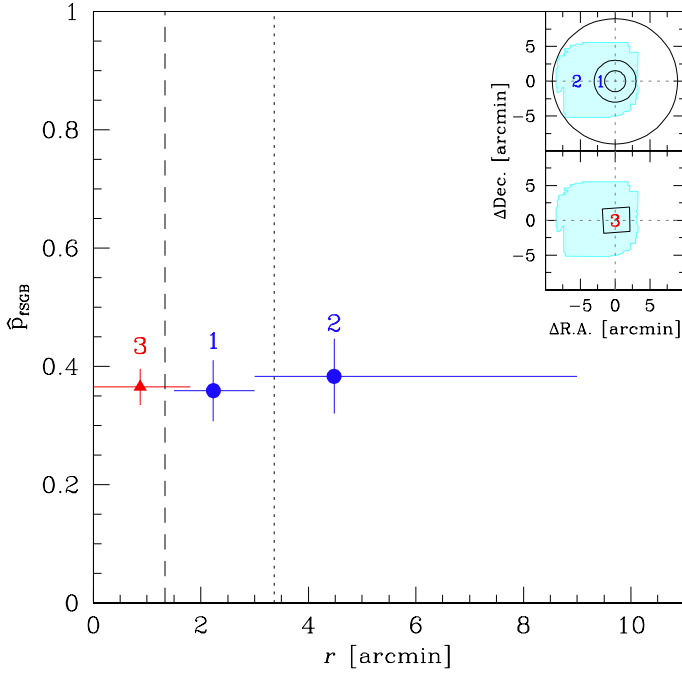


**Fig. 23.** Radial trend of  $\hat{p}_{\text{ISGB}}$ . The numbers 1, 2, and 3 correspond to panels c) in Fig. 22. The points are placed at the average distance of the SGB stars used to compute the ratio in each radial bin. In blue, we plot the ratios obtained with the HAWK-I data set; in red, we show the ratio obtained with the HST data set. The vertical error bars are computed as described in the text. The horizontal error bars cover the radial intervals. The two vertical lines indicate the core radius and half-light radius (1'.33 and 3'.36 respectively; from Harris 1996, 2010 edition). In the top-right panels, the cyan region highlights the HAWK-I field. The cluster center is set at (0, 0). The three circles have radius 1.5, 3.0, and 9.0 arcmin. The black parallelogram represents the field covered by the HST data. The regions used to compute the ratios are labeled with the numbers 1, 2, and 3, respectively.

### 9.3. NGC 6121 proper motion

As before, we chose all WFI images with an exposure time of about 180 s and only used the chips overlapping HAWK-I data. In this way, we had 36 catalogs for the first epoch. For the second HAWK-I epoch, we had 400 catalogs (100 images  $\times$  4 chips). Using local transformations, we iteratively computed the star's displacements.

The resulting CMD and VPD are shown in Fig. 24. We only show here the best-measured stars. Unfortunately, the stars fainter than  $J \sim 18.5$  in the NIR catalogs were not detectable in the optical-band WFI images. Even though the lower part of the CMD is poorly sampled (near the MS kink at  $K_S \sim 17.5$ ), the separation between cluster and field objects is still good. Cluster members are those within 4  $\text{mas yr}^{-1}$  of the cluster mean motion, while we drew an ellipse centered at (9.5, 14.0)  $\text{mas yr}^{-1}$  with major and minor axes of 17.6 and 14.3  $\text{mas yr}^{-1}$  for field stars (right VPD), respectively.

Unlike NGC 6656, we did not estimate the differential chromatic refraction effects, since the color baseline is not large enough to study the effect using only unsaturated stars. Saturated stars' proper motions are less precise, and we could confuse differential chromatic refraction with systematic trends in saturated stars' proper motions.

### 9.4. Cluster membership probability

For the two globular clusters with new proper motions, NGC 6656 and NGC 6121, we calculated cluster membership probability,  $P_\mu$ , for each star. Recently, these two clusters have been analyzed by Zloczewski et al. (2012) but, instead of giving membership probabilities, these authors simply divided all stars with measured proper motions into field stars, possible cluster members, and likely cluster members. This approach can be justified on the grounds of a clear separation between field and cluster in the VPD (Figs. 21, 24). However, a more rigorous cluster membership calculation technique would help to better characterize each star's membership probability. We selected a well-tested local sample method (e.g., van Altena 2013, Chap. 25). In this method, a limited subset of stars is selected for each target star with properties close to those of a target. Then, a cluster membership probability,  $P_\mu$  of a star is calculated using the density functions defined by the local sample. This approach delivers more accurate membership probabilities over the entire range of magnitudes. In the case of globular clusters, the potential bias in  $P_\mu$  at various magnitudes is less significant because the cluster stars dominate a relatively small number of field stars. In the presence of a highly varying precision of calculated proper motions (ranging from 0.2 to 5.5  $\text{mas yr}^{-1}$  for NGC 6656 and NGC 6121), however, using an aggregate density function for a cluster and field can produce unreliable membership probabilities for low-precision proper motions. This is due to a significant widening of cluster's density function at the low-precision end of proper motions. Therefore, we adopted the mean error  $\sigma_\mu$  of proper motions as a single parameter allowing us to find a local sample, which is similar to what was applied to the catalog of proper motions in  $\omega$  Cen (Paper III). There are a few differences from the study of  $\omega$  Cen. First, we used a fixed window in the error distributions with the total width not exceeding 0.75  $\text{mas yr}^{-1}$  so that a target star is located in the middle of this window. The total number of stars in local sample never exceeds 3000, hence the window size for well-measured proper motions, which dominate the catalog, can be as small as 0.1  $\text{mas yr}^{-1}$ . At the extreme values of proper-motion errors, the window size is fixed and the placement of a target may no longer be in the middle of this window. Second, we used a modified mean  $\sigma_\mu = \sqrt{(\mu_\alpha \cos \delta)^2 + \mu_\delta^2} / \sqrt{2}$ . Third, the Gaussian width of a cluster density function was interpolated by using an empirical relationship:  $\sigma_c = (0.04 \times (K_S - 12) + 1) \times \sigma_\mu$ , where  $K_S$  is the measured NIR magnitude of a target star. In addition,  $\sigma_c$  was never let to be lower than 0.7  $\text{mas yr}^{-1}$ .

While the cluster density function is always a 2D Gaussian, it is often convenient to use a flat sloping density function for the field-star distribution in the VPD. This is related to the binning of VPD. The adopted size of a binning area, centered on the cluster, is  $5\sigma_c \times 5\sigma_c$  which formally should contain all cluster members. If a star's  $\sigma_\mu < 2 \text{ mas yr}^{-1}$ , then it also means that the binning area never reaches the center of a field-star centroid in the VPD for both globular clusters. In the regime of high proper motion errors ( $>3 \text{ mas yr}^{-1}$ ), the distribution of field stars is so diffuse that a significant portion of its wings falls outside the VPD area covered by proper motions. The few free parameters of both cluster and field density distributions,  $\Phi_c$  and  $\Phi_f$ , are calculated according to Kozhurina-Platais et al. (1995) but the resulting cluster membership probability  $P_\mu$  is defined by Eq. (25.8) from van Altena (2013).

We note that likely clusters stars have  $P_\mu > 75\%$ , but almost certain field stars have  $P_\mu < 1\%$ . The stars with intermediate

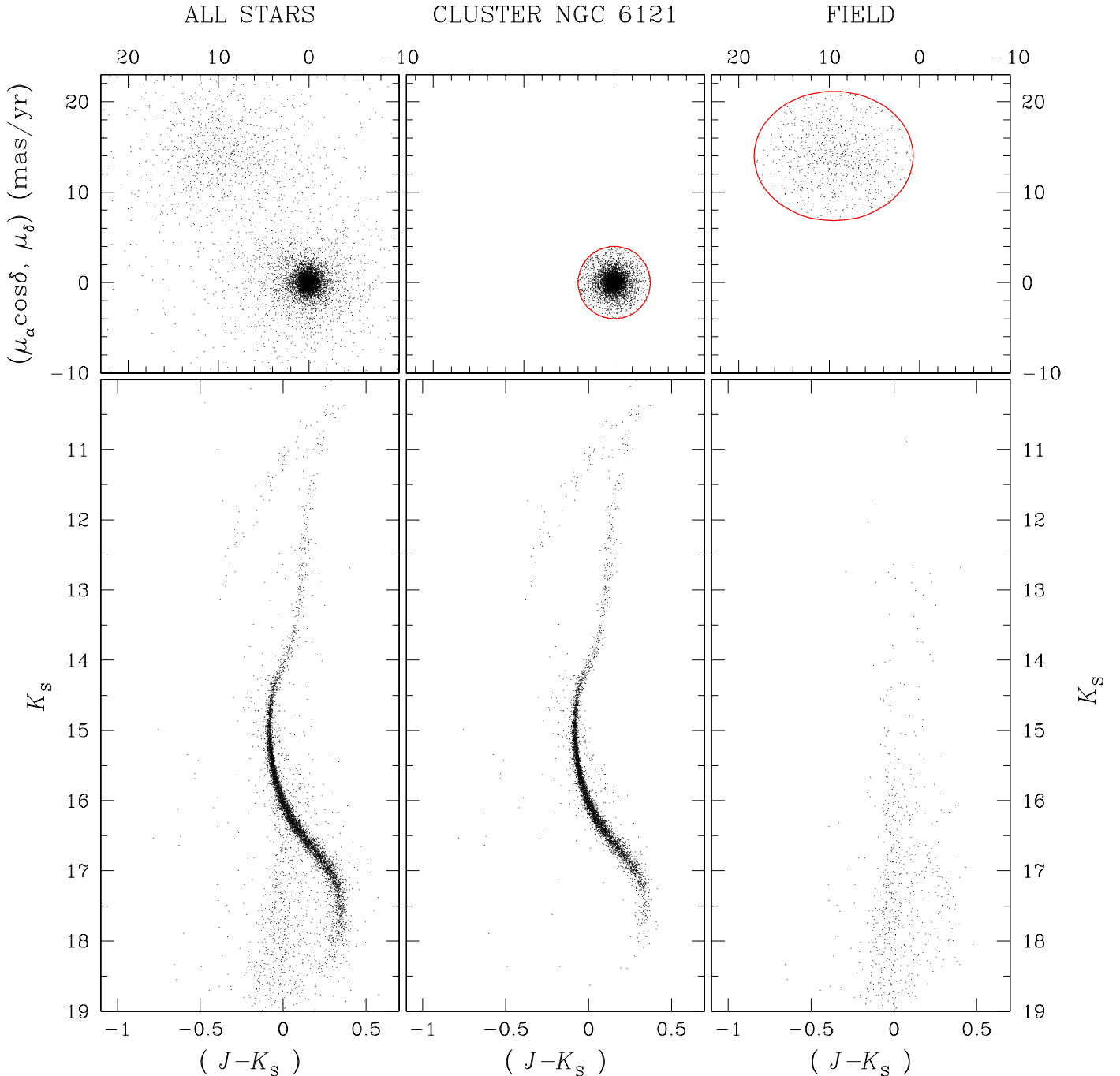


**Fig. 24.** Same as Fig. 21 but for NGC 6121. The radius of the circle centered on the origin of the VPD is  $4 \text{ mas yr}^{-1}$ , while the ellipse in the right VPD defining probable field stars is centered at  $(9.5, 14.0) \text{ mas yr}^{-1}$  with major and minor axes of  $17.6$  and  $14.3 \text{ mas yr}^{-1}$ , respectively. The ellipse mainly encloses stars in the outer part of the Bulge.

membership probabilities are more likely to be cluster members than field stars. This follows from the fact that the respective centroids in the VPD have a significant separation and that there is a relatively small fraction of field stars among all stars with measured proper motions, namely  $\sim 24\%$  for NGC 6656 and  $\sim 9\%$  for NGC 6121. This should be considered when examining the astrometric cluster membership of rare stars, such as variables, blue stragglers, and horizontal branch stars.

#### 9.4.1. Membership of variables in NGC 6656

Kaluzny & Thompson (2001) published a catalog of 36 variable stars in the central field of NGC 6656. We cross-identified

these sources in our catalog and found 27 stars in our proper motion catalog. In Table 4, we report the membership probability for these stars ( $ID_{KT}$  are Kaluzny & Thompson labels;  $ID_{L13}$  are the identification labels in our catalog.). In Fig. 25, we show  $V$  vs.  $(V - K_S)$  CMD (bottom-left panel),  $V$  vs.  $P_\mu$  (bottom-right panel) and the VPD (top panel) for all stars in our sample with a membership probability measure. We set two thresholds in  $P_\mu$  ( $P_\mu = 2\%$  and  $P_\mu = 75\%$ ) and divided our catalog in three samples: likely-field stars with  $P_\mu < 2\%$ , dubious membership stars with  $2\% \leq P_\mu < 75\%$  and likely cluster members with  $P_\mu \geq 75\%$ . Eleven stars have  $P_\mu < 2\%$  (green triangles); two stars have  $2\% \leq P_\mu < 75\%$  (yellow squares), and the remaining 14 stars have  $P_\mu \geq 75\%$  (azure circles). The

**Table 4.** Membership probability for the NGC 6656 variable star catalog of Kaluzny & Thompson (2001).

ID <sub>KT</sub>	ID <sub>L13</sub>	$P_\mu$	ID <sub>KT</sub>	ID <sub>L13</sub>	$P_\mu$
Members					
M22_V02	45566	99	M22_V29	161746	96
M22_V04	56333	99	M22_V33	181768	86
M22_V10	93320	89	M22_V34	181631	80
M22_V16	104996	98	M22_V36	185551	84
M22_V20	131248	99	M22_V45	155768	79
M22_V23	144995	95	M22_V51	77720	95
M22_V28	155692	87	M22_V55	148685	94
Probably members					
M22_V14	102946	2	M22_V37	193535	37
Non members					
M22_V03	47877	0	M22_V18	113038	0
M22_V05	57746	0	M22_V42	79935	0
M22_V07	68695	0	M22_V46	157407	0
M22_V08	74698	0	M22_V48	183116	0
M22_V12	101344	0	M22_V54	138212	0
M22_V15	106319	0			

**Notes.** ID<sub>KT</sub> is the ID used in Kaluzny & Thompson (2001), and ID<sub>L13</sub> is in our catalog.

two variable stars with  $2\% \leq P_\mu < 75\%$ , namely M22\_V37 and M22\_V14, are saturated horizontal-branch stars for which the motion is generally consistent with the cluster’s mean motion. As we stated in Sect. 9.4, they should be considered likely cluster members although their formal membership probabilities are below 75%. Note that not all the saturated stars could have well-measured proper motion due to the less-accurate PSF-fitting process and less-constrained positions (QFIT could be higher than 0.1). Saturated stars (while they will have less precise astrometry) are of intrinsic interest, since they are the best candidates for follow-up spectroscopy if identified as cluster members. Nonetheless, caution must be taken in interpreting their astrometry.

#### 9.4.2. Membership of variables in NGC 6121

We can similarly use our proper motion data to assign membership probabilities to candidate variable star members of NGC 6121. Shokin & Samus (1996) cataloged 53 NGC 6121 variable stars from the literature and provided equatorial coordinates. We cross-checked our proper motion catalog with that provided by the authors, and we found 42 sources in common. Figure 26 shows these variable stars in  $J$  vs.  $(B - J)$  CMD and VPD. As for NGC 6656, we set two thresholds at  $P_\mu = 2\%$  and  $P_\mu = 75\%$ , dividing our catalog in three samples. The membership probabilities are listed in Table 5 (ID<sub>S</sub> and ID<sub>L13</sub> are the labels in Shokin & Samus and in this paper, respectively.). All cross-identified variable stars are saturated in our proper motion catalog. Five stars (V6, V7, V11, V19, and V31) have  $2\% \leq P_\mu < 75\%$ . For these stars, the same considerations we made for M22\_V37 and M22\_V14 should be applied. All the known variable stars in NGC 6121 seem to be horizontal-branch stars. As field contamination is small in that portion of the CMD, their membership is strengthened considering that these are poorly-measured saturated stars.

**Table 5.** Membership probability for the NGC 6121 variable star catalog of Shokin & Samus (1996).

ID <sub>S</sub>	ID <sub>L13</sub>	$P_\mu$	ID <sub>S</sub>	ID <sub>L13</sub>	$P_\mu$
Members					
V1	176589	99	V28	30831	99
V2	173396	98	V30	16737	99
V5	164050	97	V36 (NE)	167082	91
V8	148455	87	V36 (SW)	167583	96
V9	146061	92	V37	125921	94
V10	136435	93	V38	119757	98
V12	129429	98	V39	111350	99
V14	127336	91	V41	87105	99
V15	123997	99	A381	98514	95
V16	121622	78	A382	96072	99
V18	111157	95	A505	98523	85
V20	107627	98	A519	112683	99
V22	100193	93	L1610	142443	87
V24	94766	91	L1717	115979	96
V25	87432	97	L2630	155330	98
V26	76423	86	L3602	60119	99
V27	68948	97	L3732	97216	85
Probably members					
V6	149664	39	V19	109197	20
V7	149106	6	V31	14721	71
V11	133287	41			
Non members					
V17	114412	0	A246	174902	0
V23	98450	0			

**Notes.** ID<sub>S</sub> is the ID used in Shokin & Samus (1996); ID<sub>L13</sub> is in our catalog.

## 10. Catalogs

We constructed eight different catalogs for our seven fields. We split the Baade’s Window field into two different catalogs (Bulge#1 and the rotated Bulge#2). These catalogs are electronically available in the VizieR on-line database<sup>6</sup>.

We also converted pixel-based coordinates into equatorial coordinates using the UCAC4 catalog as reference. We only used bright, unsaturated stars to compute the coefficients of the 6-parameter linear transformation between HAWK-I and UCAC4 frames. The choice of using 6-parameter linear transformations (see Sect. 5.5 for a description of these transformations) to transform star positions in our catalogs into the UCAC 4 reference system allows us to solve not only for shift, orientation, and scale, but it also minimizes most of the telescope+optics-system residuals, as well as most of the atmospheric refraction effects. Furthermore, linking our catalogs to the UCAC 4 catalog, we did not only provide the equatorial coordinates for all stars but we determined the linear terms of our distortion. The equatorial coordinates are truly our best calibrated coordinates.

The first eight columns are the same in all catalogs. Column (1) contains the ID of the star; Cols. (2) and (3) give J2000.0 equatorial coordinates in decimal degrees. Note that positions are given at the epoch of HAWK-I observations because of proper motion. Columns (4) and (5) contain the pixel

<sup>6</sup> <http://vizier.u-strasbg.fr/viz-bin/VizieR>

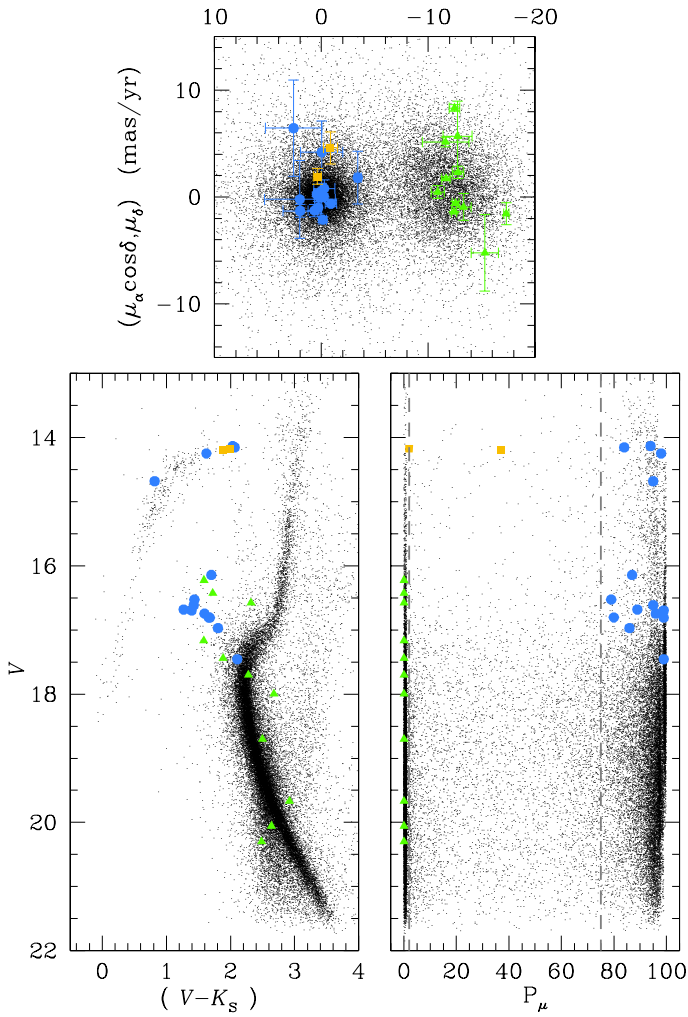


**Fig. 25.** *Bottom-left panel:* NGC 6656  $V$  vs.  $(V - K_S)$  CMD for all stars in our catalog (black dots) that have a membership probability measure. We plotted variable stars from Kaluzny & Thompson (2001) with green triangles that are cross-identified in our catalog with  $P_\mu < 2\%$ ; yellow squares represent the star with  $2\% \leq P_\mu < 75\%$ . The azure circles are those stars with  $P_\mu \geq 75\%$ . *Bottom-right panel:*  $V$  vs.  $P_\mu$ . *Top:* VPD. We also drew proper motion error bars for matched variable stars.

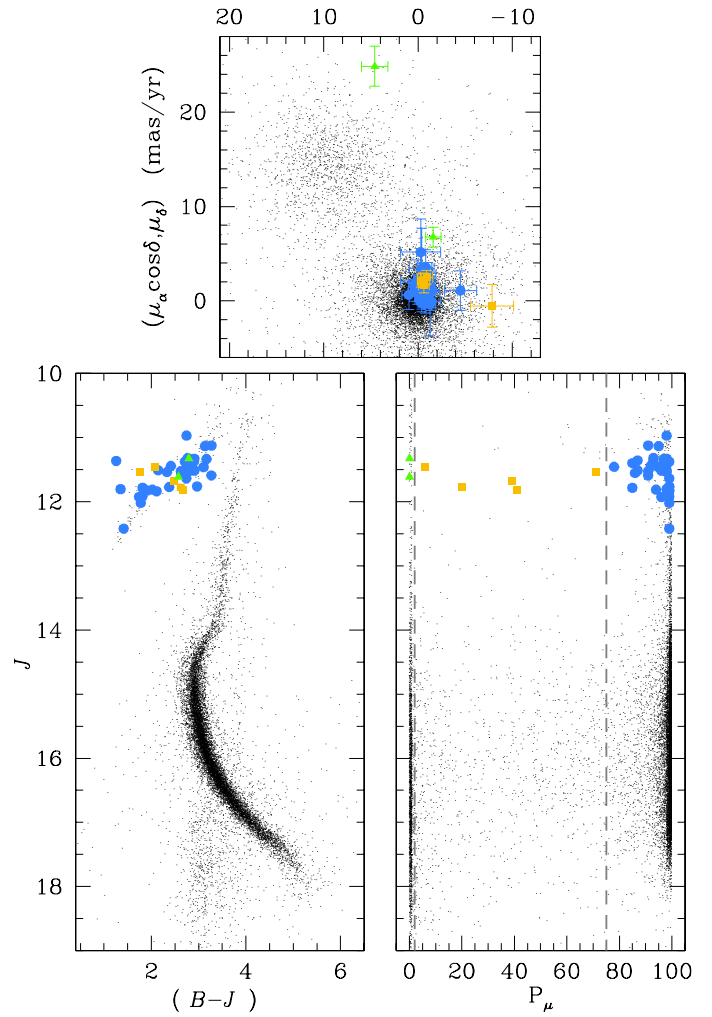


**Fig. 26.** *Bottom-left panel:* NGC 6121  $J$  vs.  $(B - J_S)$  CMD for all stars with a membership probability measure. As in Fig. 25, all stars are shown with black dots. We used azure circles, yellow squares, and green triangles to highlight cross-identified stars in the Shokin & Samus (1996) with  $P_\mu \geq 75\%$ ,  $2\% \leq P_\mu < 75\%$ , and  $P_\mu < 2\%$ , respectively. *Bottom-right panel:*  $J$  vs.  $P_\mu$ . *Top:* VPD. We show proper motion error bars for Shokin & Samus variable stars. Star V17 ( $P_\mu = 0\%$ ) is not shown because it lies outside the VPD.

coordinates  $x$  and  $y$  of the distortion-corrected reference frame. Columns (6) and (7) contain the corresponding positional rms; Col. (8) gives the number of images where the star was found.

Columns (9) and the following columns contain the photometric data and proper motions when present. Values are flagged to  $-1$  when their measures are not available with the only exception of the proper motions and their errors, for which we set to 99. Table 6 lists all columns contained in the Bulge#1 catalog. Tables 7 to 10 only contain those columns that are not in common. In the following subsections, we describe more in detail the remaining columns (9+) of each catalog.

*Baade's Window (Bulge#1).* Columns (9) to (23) contain the photometric data: i.e.,  $J$ ,  $H$ ,  $K_S$  (both with 2MASS- and MKO-based zero-points added), their errors, the number of images used to compute the magnitude of the star in the master frame, and the QFIT in this order. Columns (24) and (25) contain a flag to weed out PSF artefacts from the  $J$  and  $H$  filter (see Sect. 7).

All stars in this catalog have a measure of the magnitude in  $K_S$  filter.

*NGC 6822, NGC 6388, LMC, and 47 Tuc.* Columns (9) to (18) contain the  $J$  and  $K_S$  photometric data; Cols. (19) and (20) contain the weed-out flags (see Table 7). In the NGC 6822, LMC, and 47 Tuc catalogs, all stars have a  $J$ -magnitude measurement, and NGC 6388 has a  $K_S$ -magnitude measurement.

*Baade's Window rotated by  $135^\circ$  (Bulge#2).* Columns (9) to (14) contain  $K_S$  magnitudes, errors, the number of stars used to compute the average magnitudes, QFIT and the weed-out flag values, respectively (Table 8).

*NGC 6656.* Columns (9) to (26) contain the photometric data in  $K_S$ ,  $B$ ,  $V$ , and  $I$  band. Finally, Columns (27) to (31) contain the proper motion data:  $\mu_\alpha \cos \delta$  (27),  $\sigma_{\mu_\alpha \cos \delta}$  (28),  $\mu_\delta$  (29),  $\sigma_{\mu_\delta}$  (30), and the number of pairs of images in which a given star's

**Table 6.** Bulge#1 catalog.

Column #	Name	Description
(1)	ID	ID number of the star
(2)	$\alpha$	Right Ascension [°]
(3)	$\delta$	Declination [°]
(4)	$x$	$x$ -master frame position [pixel]
(5)	$y$	$y$ -master frame position [pixel]
(6)	$\sigma_x$	rms error in the $x$ -position [pixel]
(7)	$\sigma_y$	rms error in the $y$ -position [pixel]
(8)	$n_{\text{pos}}$	Number of images where the star was found in used to compute the master-frame position
(9)	$J$	Calibrated $J$ magnitude in 2MASS system
(10)	$H$	Calibrated $H$ magnitude in 2MASS system
(11)	$K_S$	Calibrated $K_S$ magnitude in 2MASS system
(12)	$J$	Calibrated $J$ magnitude in MKO system
(13)	$H$	Calibrated $H$ magnitude in MKO system
(14)	$K_S$	Calibrated $K_S$ magnitude in MKO system
(15)	$\sigma_J$	rms error in $J$ photometry
(16)	$\sigma_H$	rms error in $H$ photometry
(17)	$\sigma_{K_S}$	rms error in $K_S$ photometry
(18)	$n_J$	Number of images where the star was found in used to compute the $J$ magnitude
(19)	$n_H$	Number of images where the star was found in used to compute the $H$ magnitude
(20)	$n_{K_S}$	Number of images where the star was found in used to compute the $K_S$ magnitude
(21)	QFIT $_J$	Quality of $J$ PSF-fit
(22)	QFIT $_H$	Quality of $H$ PSF-fit
(23)	QFIT $_{K_S}$	Quality of $K_S$ PSF-fit
(24)	weed $_J$	$J$ weed-out flag (1 = star, 0 = PSF-artefact, -1 = star not found in $J$ exposures)
(25)	weed $_H$	$H$ weed-out flag

**Table 7.** NGC 6822, NGC 6388, LMC and 47 Tuc catalogs.

Column #	Name	Description
(...)	(...)	(...)
(9)	$J$	Calibrated $J$ magnitude in 2MASS system
(10)	$K_S$	Calibrated $K_S$ magnitude in 2MASS system
(11)	$J$	Calibrated $J$ magnitude in MKO system
(12)	$K_S$	Calibrated $K_S$ magnitude in MKO system
(13)	$\sigma_J$	rms error in $J$ photometry
(14)	$\sigma_{K_S}$	rms error in $K_S$ photometry
(15)	$n_J$	Number of images where the star was found in used to compute the $J$ magnitude
(16)	$n_{K_S}$	Number of images where the star was found in used to compute the $K_S$ magnitude
(17)	QFIT $_J$	Quality of $J$ PSF-fit
(18)	QFIT $_{K_S}$	Quality of $K_S$ PSF-fit
(19)	weed $_J$	$J$ weed-out flag (1 = star, 0 = PSF-artefact, -1 = star not found in $J$ exposures)
(20)	weed $_{K_S}$	$K_S$ weed-out flag

**Table 8.** Bulge#2 catalog.

Column #	Name	Description
(...)	(...)	(...)
(9)	$K_S$	Calibrated $K_S$ magnitude in 2MASS system
(10)	$K_S$	Calibrated $K_S$ magnitude in MKO system
(11)	$\sigma_{K_S}$	rms error in $K_S$ photometry
(12)	$n_{K_S}$	Number of images where the star was found in used to compute the $K_S$ magnitude
(13)	QFIT $_{K_S}$	Quality of $K_S$ PSF-fit
(14)	weed $_{K_S}$	$K_S$ weed-out flag (1 = star, 0 = PSF-artefact, -1 = star not found in $K_S$ exposures)

proper motion was measured (31). Finally, Col. (32) contains the membership probability (Table 9). Stars measured in only one exposure in either  $B$ ,  $V$ , or  $I$  filters have photometric rms values of 9.9. As for Bulge#1, all stars have a measure of the magnitude in  $K_S$  filter.

*NGC 6121*. Columns (9) to (32) contain the photometric data in  $J$ ,  $K_S$ ,  $B$ ,  $V$ , and  $Rc$  bands. Columns (33) to (37) contain the proper motion data and Col. (38) is the membership probability (Table 10). As in the NGC 6656 catalog, a rms equal to 9.9 is used for those stars measured in only 1 exposure in  $K_S$ ,

Table 9. NGC 6656 catalog.

Column #	Name	Description
(...)	(...)	(...)
(9)	$K_S$	Calibrated $K_S$ magnitude in 2MASS system
(10)	$K_S$	Calibrated $K_S$ magnitude in MKO system
(11)	$B$	Calibrated $B$ magnitude
(12)	$V$	Calibrated $V$ magnitude
(13)	$I$	Calibrated $I$ magnitude
(14)	$\sigma_{K_S}$	rms error in $K_S$ photometry
(15)	$\sigma_B$	rms error in $B$ photometry
(16)	$\sigma_V$	rms error in $V$ photometry
(17)	$\sigma_I$	rms error in $I$ photometry
(18)	$n_{K_S}$	Number of images where the star was found in used to compute the $K_S$ magnitude
(19)	$n_B$	Number of images where the star was found in used to compute the $B$ magnitude
(20)	$n_V$	Number of images where the star was found in used to compute the $V$ magnitude
(21)	$n_I$	Number of images where the star was found in used to compute the $I$ magnitude
(22)	QFIT $_{K_S}$	Quality of $K_S$ PSF-fit
(23)	QFIT $_B$	Quality of $B$ PSF-fit
(24)	QFIT $_V$	Quality of $V$ PSF-fit
(25)	QFIT $_I$	Quality of $I$ PSF-fit
(26)	weed $_{K_S}$	$K_S$ weed-out flag (1 = star, 0 = PSF-artefact, -1 = star not found in $K_S$ exposures)
(27)	$\mu_\alpha \cos \delta$	Proper-motion value along $\mu_\alpha \cos \delta$ [mas yr $^{-1}$ ]
(28)	$\sigma_{\mu_\alpha \cos \delta}$	rms of $\mu_\alpha \cos \delta$ [mas yr $^{-1}$ ]
(29)	$\mu_\delta$	Proper-motion value along $\mu_\alpha \cos \delta$ [mas yr $^{-1}$ ]
(30)	$\sigma_{\mu_\delta}$	rms of $\mu_\delta$ [mas yr $^{-1}$ ]
(31)	$n_{\text{pairs}}$	Number of pairs of first-second epoch images used to compute the proper motion of the star
(32)	$P_\mu$	Membership probability

Table 10. NGC 6121 catalog.

Column #	Name	Description
(...)	(...)	(...)
(9)	$J$	Calibrated $J$ magnitude in 2MASS system
(10)	$K_S$	Calibrated $K_S$ magnitude in 2MASS system
(11)	$J$	Calibrated $J$ magnitude in MKO system
(12)	$K_S$	Calibrated $K_S$ magnitude in MKO system
(13)	$B$	Calibrated $B$ magnitude
(14)	$V$	Calibrated $V$ magnitude
(15)	$Rc$	Calibrated $Rc$ magnitude
(16)	$\sigma_J$	rms error in $J$ photometry
(17)	$\sigma_{K_S}$	rms error in $K_S$ photometry
(18)	$\sigma_B$	rms error in $B$ photometry
(19)	$\sigma_V$	rms error in $V$ photometry
(20)	$\sigma_{Rc}$	rms error in $Rc$ photometry
(21)	$n_J$	Number of images where the star was found in used to compute the $J$ magnitude
(22)	$n_{K_S}$	Number of images where the star was found in used to compute the $K_S$ magnitude
(23)	$n_B$	Number of images where the star was found in used to compute the $B$ magnitude
(24)	$n_V$	Number of images where the star was found in used to compute the $V$ magnitude
(25)	$n_{Rc}$	Number of images where the star was found in used to compute the $Rc$ magnitude
(26)	QFIT $_J$	Quality of $J$ PSF-fit
(27)	QFIT $_{K_S}$	Quality of $K_S$ PSF-fit
(28)	QFIT $_B$	Quality of $B$ PSF-fit
(29)	QFIT $_V$	Quality of $V$ PSF-fit
(30)	QFIT $_{Rc}$	Quality of $Rc$ PSF-fit
(31)	weed $_J$	$J$ weed-out flag (1 = star, 0 = PSF-artefact, -1 = star not found in $J$ exposures)
(32)	weed $_{K_S}$	$K_S$ weed-out flag
(33)	$\mu_\alpha \cos \delta$	Proper-motion value along $\mu_\alpha \cos \delta$ [mas yr $^{-1}$ ]
(34)	$\sigma_{\mu_\alpha \cos \delta}$	rms of $\mu_\alpha \cos \delta$ [mas yr $^{-1}$ ]
(35)	$\mu_\delta$	Proper-motion value along $\mu_\alpha \cos \delta$ [mas yr $^{-1}$ ]
(36)	$\sigma_{\mu_\delta}$	rms of $\mu_\delta$ [mas yr $^{-1}$ ]
(37)	$n_{\text{pairs}}$	Number of pairs of first-second epoch images used to compute the proper motion of the star
(38)	$P_\mu$	Membership probability

$B$ ,  $V$ , or  $R_c$  filter. In this catalog, all stars have a  $J$ -magnitude measurement.

## 11. Conclusion

We derived an accurate distortion solution in three broad band filters for the HAWK-I detector and release the tools to correct the geometric distortion with our solution. We also produced astro-photometric catalogs of seven stellar fields. We release catalogs with astrometric positions, photometry, proper motions, and membership probabilities of NGC 6121 (M 4) and NGC 6656 (M22), while the remaining fields (the Baade’s window, NGC 6822, NGC 6388, NGC 104, and the JWST calibration field) studied in the present paper only contains astrometry and photometry. These catalogs are useful for selecting spectroscopic targets, and can serve as distortion-free frames with respect to which one can solve for the geometric distortion of present/future imagers. The astronomical community has started to focus its attention on wide-field cameras equipped with NIR detectors, and the quantity and quality of NIR devices have improved considerably. This is a first effort to develop the expertise with these detectors to fully exploit the data coming from large-field NIR surveys, such as the VVV survey taken with VIRCAM at VISTA. Finally, an additional goal of this work is to get ready for the upcoming JWST, whose imagers define the state-of-the-art in astrometry, in particular in crowded environments not reachable by *Gaia*.

We analyzed both photometric and astrometric performance of the NIR mosaic HAWK-I@VLT using images of seven different fields observed during commissioning in 2007. We computed a geometric-distortion solution for each chip of HAWK-I in three different broad band filters ( $J$ ,  $H$ ,  $K_S$ ). Our dithered-observation strategy using the self-calibration technique allowed us to randomize the systematic errors and to compute the average stars’ positions that provide an approximation of the true positions in the distortion-free master frame. A fifth-order polynomial solution highlighted a periodic pattern in the distortion residuals. We have demonstrated that this pattern is not a geometric effect (as it is the case for the WFPC2 or the WFC3/UVIS@HST) but it is a periodic lag introduced by alternating readout amplifiers. To remove it, we used a square-wave function and a 64-pixel step table of residuals. Finally we used four additional look-up tables (one per chip) to perform a bi-linear interpolation to take all uncorrected residuals into account and to further improve our solutions. Thanks to our 5-step distortion correction, we are able to reach a positional rms of  $\sim 3.5$  mas in each coordinate. Using a general 6-parameter linear transformations to match-up different images, the effects due to telescope+instrument and atmosphere are absorbed, and the  $\sigma$ (Radial residual) further decreases, reaching  $\sim 2.8$  mas under good seeing conditions. We emphasize that this is a relative positioning precision – i.e., it indicates how accurately we can measure the differential position of a star in multiple images of the same field.

We have also shown that the non-linear terms of our distortion solution can be transferred between observing runs at the 10 mas level. The astrometric accuracy contained in the pixel-coordinate system degrades moving toward the edges of the FoV because the stars’ positions were obtained as the average of fewer images than in the center of the field. Therefore, the average positions are more vulnerable to poorly-constrained transformations of the individual exposures into the master frame. The accuracy can decrease from  $\sim 10$  mas to  $\sim 100$  mas ( $\sim 1$  pixel) going from the center to the edges of the FoV. For this reason, we advise to use the inner part of the detector for high-precision

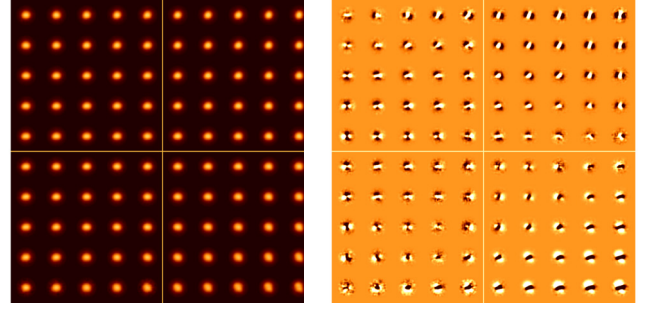


**Fig. A.1.** *Left:*  $10 \times 10$  PSFs for the whole HAWK-I detector ( $5 \times 5$  PSFs per chip). *Right:* spatial variation of the PSFs. To each local PSF, we subtracted a single average PSF for the whole detector. A darker color means less flux than the average PSF, and a lighter color means more flux.

astrometry. To achieve a higher astrometric accuracy, we also advise to link the pixel-coordinate catalog to a reference frame such as UCAC 4 to determine the linear terms of the distortion. Finally local transformations (as those used to compute the proper motion in Sect. 9) should be used to minimize the effects of residuals in the geometric distortion corrections as described in Paper I.

In the second part of the paper, we showed the potential applications of our astrometric techniques and computed the *relative* proper motion of stars in the field of the globular clusters NGC 6656 and NGC 6121. With a time baseline of about 8 years, we have clearly separated cluster members from field stars. Accuracy of proper-motion measurements is limited by the depth and the precision of first-epoch data set. We note that the stellar positions in our catalogs have been derived from only a single epoch of HAWK-I data. A second-epoch HAWK-I (or another wide-field infrared camera) data set is needed to provide proper-motion solutions that allow these data to be extended with confidence to arbitrary future epochs. We exploit photometry and proper motions of stars in NGC 6656 to study its stellar populations. We find that the bimodal SGB, previously discovered from visual and ultraviolet HST photometry (Piotto et al. 2012), is also visible in the  $K_S$  versus  $(B - K_S)$  CMD. We combined information from HAWK-I observation of the outer part of NGC 6656 and from HST images of the innermost cluster region (Piotto et al. 2012) to study the radial distribution of the two SGBs. To do this, we calculated the number ratio of the faint SGB  $\hat{\rho}_{\text{ISGB}}$  for stars at different radial distances from the cluster center to  $9'$  ( $\sim 6.8$  core radii). We found that the two SGBs have the same radial distribution within our uncertainty.

*Acknowledgements.* M.L. and G.P. acknowledge partial support from the Università degli Studi di Padova CPDA101477 grant. M.L. acknowledges support from the STScI under the 2013 DDRF program. A.P.M. acknowledges financial support from the Australian Research Council through Discovery Project grant DP120100475. We thank Dr. Jay Anderson for careful reading of the manuscript and for thoughtful comments. We thank the anonymous referee for the useful comments and suggestions that considerably improved the quality of our paper.

## Appendix A: Study of the HAWK-I PSF

### A.1. PSF spatial variability

As in the case of the WFI@2.2 m (Paper I), the PSF shape for the HAWK-I@VLT detector is different from one chip to the other and from side to side within the same chip. To fully take this spatial variation into account, we decided to solve for an array

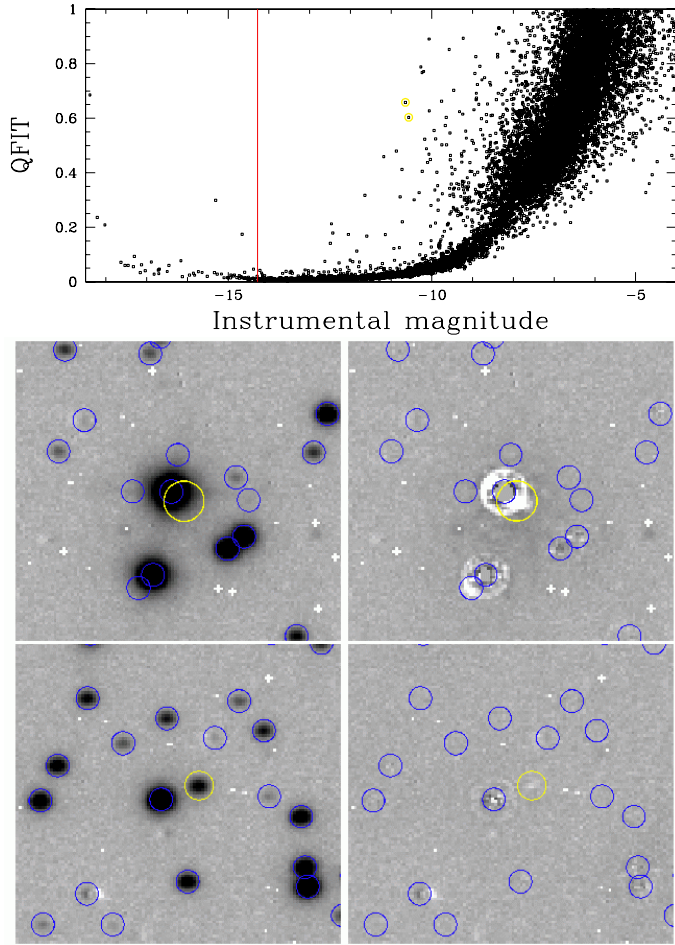


**Fig. A.2.** *Top:* QFIT parameter as a function of the instrumental magnitude  $J$  for chip[1] of exposure HAWKI.2007-08-03T01:41:29.785.fits. In yellow, we highlighted two sources with anomalously high QFIT. The red line shows the saturation limit. *Middle/bottom-left:* location of the two sources (in yellow) on the image. Blue circles mark all stars for which we were able to measure a position and a flux. White pixels are those flagged according to the bad-pixel mask. We do not find stars too close to these bad pixels. *Middle/bottom-right:* the corresponding subtracted images. The first of the two high-QFIT stars (*middle-right panel*) we selected is in close proximity to a saturated star; it has been poorly measured and therefore has a large QFIT value. The second star (*bottom-right panel*) has a cosmic ray event close to its center, increasing its total apparent flux and shifting its center on the image. This star has been over-subtracted, resulting again in a larger QFIT value.

of 25 PSFs per chip (5 across and 5 high). A bi-linear interpolation is used to derive the proper PSF model in each location of the detector (see Paper I). The left panel of Fig. A.1 shows these  $5 \times 5$  PSFs for the whole HAWK-I detector. At a first glance, we can already see that the PSFs' shape and orientation vary across the detector (especially close to the edge). To better quantify the size of these variations, we built a single, average PSF for the whole detector, and we subtracted it to each of the local PSFs. The result is shown on the right panel of the Fig. A.1. The actual spatial variation of the PSF is indeed large, even between two adjacent PSFs. The darker color of Fig. A.1 means less flux than the average PSF, while a lighter one means more flux. The maximum variation of the local PSF with respect to the average one is 0.02%.

In sparse fields (or short exposures), there might not be enough bright and isolated stars to build the full  $5 \times 5 \times 4 = 100$

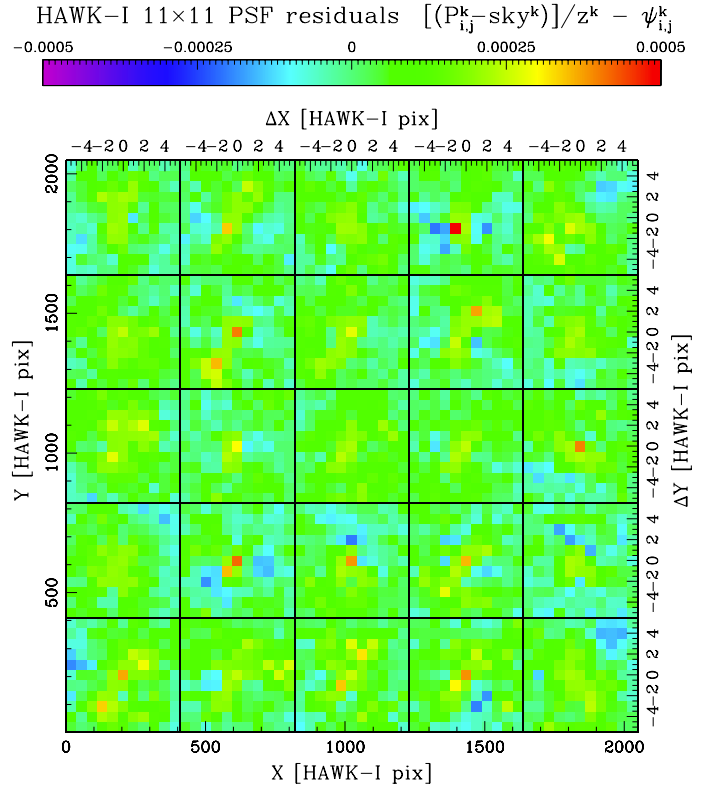


**Fig. A.3.** PSF spatial variability for chip[1]. Pixel values are color-coded as shown on top.

set of PSFs. We customized the software to allow for different PSF-array solutions: (1) one PSF per chip; (2) four PSFs per chip (at the corners); (3) six PSFs per chip; (4) nine PSFs per chip; and (5) the full  $5 \times 5$  array. The user can choose to include fainter and more crowded stars to model the PSF to increase the statistics of each PSF model. According to the crowding of the field of interest and the image quality, the user must determine the best compromise between how finely to model the PSF's spatial variability and the need to have an adequate number of stars to model each PSF. Choosing the best solution is a delicate matter. To obtain the best results, we investigated for every single exposure whether it was better to have more or less PSFs by analyzing the trend of the QFIT across the image: better PSF models provide smaller QFIT values.

The top panel of Fig. A.2 shows QFIT values as a function of the instrumental magnitude for chip[1] of exposure HAWKI.2007-08-03T01:41:29.785.fits. This is an image in the field of M 4 taken through  $J$  filter. The instrumental magnitude is defined as  $-2.5 \times \log(\sum \text{counts})$ , where  $\sum \text{counts}$  is the sum of the total counts under the fitted PSF. The red line in the figure indicates when stars start to be saturated<sup>7</sup>.

For well-exposed stars (e.g., with instrumental magnitude  $J$  between  $-14$  and  $-10$ ), QFIT values are typically below 0.05 and increase for fainter or saturated stars. However, there are a few sources with anomalously high QFIT in this interval. To find out what kind of outliers these sources are, we selected two of them (highlighted in yellow in Fig. A.2). Their location on the image is shown in the bottom-left panels of Fig. A.2 in yellow.

<sup>7</sup> The maximum central pixel value of the PSFs for this exposure is 0.058 (i.e., 5.8% of the star's flux falls within its central pixel). We set saturation to take place at 30 000 counts, which means at instrumental magnitude  $-2.5 \times \log(30\,000/0.058) \approx -14.28$ .

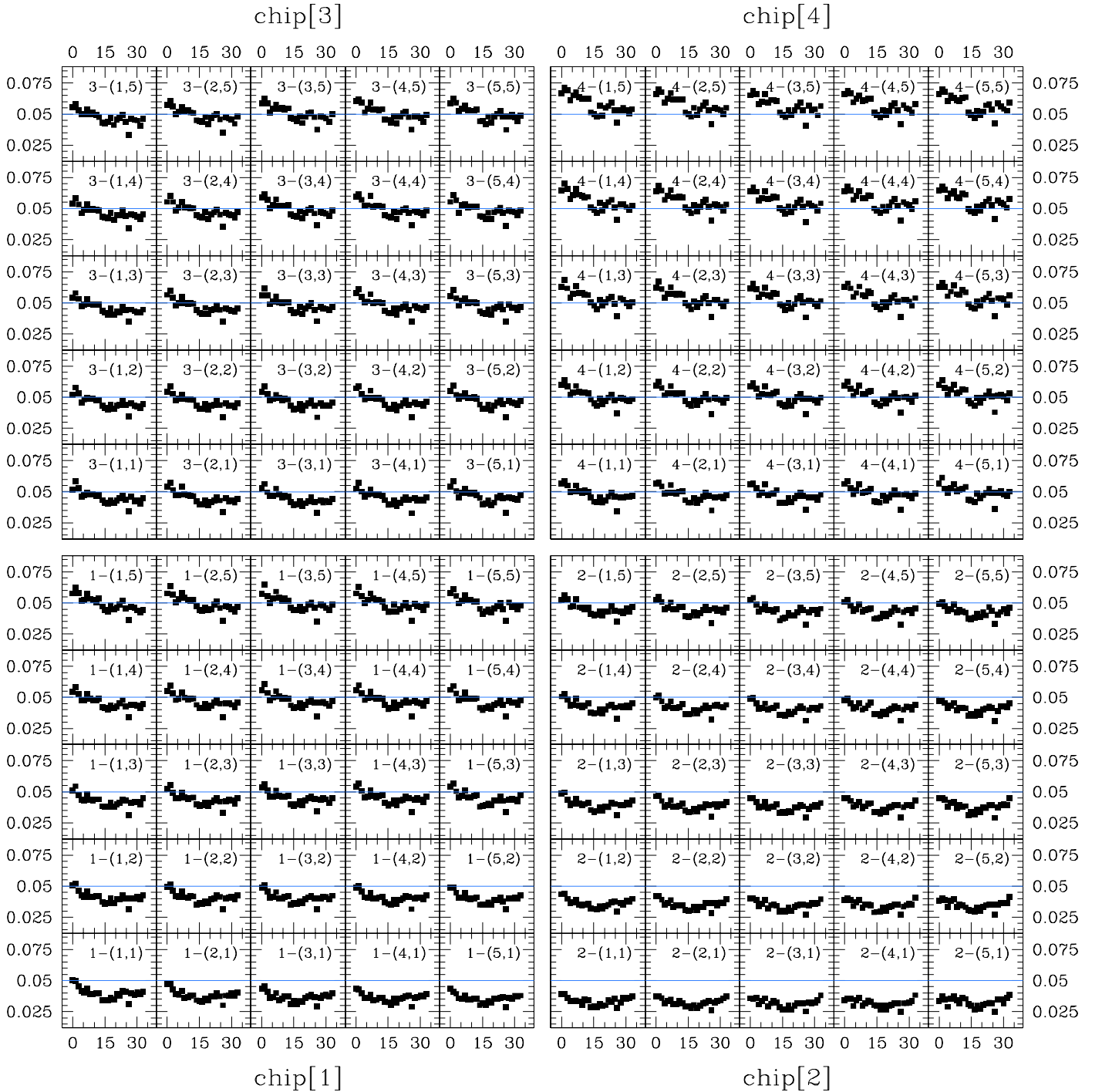


**Fig. A.4.** Central PSF values as function of the exposure sequence. We highlighted the central PSF value of 0.05 in blue.

Blue circles mark all stars for which we were able to measure a position and a flux. White pixels are those flagged using the bad-pixel mask. We did not find stars too close to these bad pixels. Bottom-right panels in the figure show the corresponding subtracted images. We can see that our PSF-fitting procedure is able to leave very small residuals in the subtracted image, except for saturated stars. The first of the two high-QFIT stars we selected (see top-right panel) is in close proximity of a saturated star; it has been poorly measured because of the light contamination from the neighboring star, and therefore has a large QFIT value. The second star has a cosmic ray event close to its center, increasing its total apparent flux and shifting its center on

the image. This star has been over-subtracted (see bottom-right panel), resulting again in a larger QFIT value.

To better quantify how our PSF models adequately represent the image. This star has been over-subtracted (see bottom-right panel), resulting again in a larger QFIT value. To better quantify how our PSF models adequately represent the image, we perform the following test. A total of 100 exposures in the field of M 4 were taken between August 3 and 5, 2007 in four runs of 25 images each. We used here only the first 25 images taken consecutively on August 3, 2007 during a time span of about 34 min. We derived an array of  $5 \times 5$  PSFs for each chip of these images. Then, we selected all the  $k$  bright, unsaturated stars (instrumental magnitude  $J < -10$ ), which have no brighter neighbors within 10 pixels, and we measured positions and fluxes for them using our  $5 \times 5$

PSF arrays. Usually, there are over 1000 such stars per chip in our exposures, uniformly distributed over the detector.

If our PSFs are well characterized, we should be able to obtain subtracted images where removed stars leave nearly no flux residuals. Therefore, the size of these residuals tell us how much our PSF models differ from real star profiles.

We extracted  $11 \times 11$  pixel rasters around each star  $k$  (i.e.,  $\pm 5$  pixels from its center) in each exposure for a total of 121  $P_{i,j}$  pixel values per star. We subtracted the local sky value to all of them, which is computed as the  $2\sigma$ -clipped median value of the counts in an annulus between 8 and 12 from the star's center. This is the net star's flux at any given location on the raster. The fractional star's flux is obtained by dividing these values by the total star's flux  $z$ . Besides Poisson errors, these values should reflect what our PSF models predict for those pixels ( $\psi_{i,j}$ ), so that we should always have in principle:

$$\frac{P_{i,j}^k - \text{sky}^k}{z^k} - \psi_{i,j}^k = 0.$$

Deviations of these values from zero tell us how much our PSFs over- or underestimate the true star's profile. Results of this test are reported in Fig. A.3 for chip[1]. We divided the  $2048 \times 2048$  pixels of the chip into  $5 \times 5$  sub-regions with one for each PSF we built. Within each area, we computed the  $3\sigma$ -median values of the residuals for each pixel of the raster. Pixel values are color-coded as shown on top of Fig. A.3. From the Fig. A.3, we can easily see that PSF residuals are in general smaller than 0.05% even in the central pixel (where Poisson noise is most effective). This proves that our spatial-dependent PSF models are able to adequately represent a star profile at any given location of the chip.

## A.2. PSF time variability

Ground-based telescopes suffer from varying seeing and airmass conditions, telescope flexures, and changes in focus. These are all effects that may severely alter the shape of the PSF. Figure A.4 illustrates how much the seeing can actually affect the PSFs. In the figure, we show the first 25 exposures of M 4 that were consecutively taken on August 3, 2007. The total time baseline is 34 min. For each of our PSF models, we considered the value of its central pixel as a function of the exposure sequence, starting from the first exposure. On average, chip[4] PSFs are sharper, while chip[2] stars have the least amount of flux in their central pixels. As a reference, we highlight a central PSF value of 0.05 (i.e., 5% of the total star's flux in its center pixel) in blue. Within the same exposures, central PSF values can range from 0.03 to 0.07 (see also Fig. A.1 for the PSF to PSF variation).

In a time span as short as half an hour, we can already see some interesting PSF time-variability effects. First of all, central PSF values vary in an inhomogeneous way across the detector. For instance, there are specific locations on the detector (e.g., the top PSFs of chip[4]) where central PSF values can change by up to 40%. On the other hand, central PSF values are more stable in different locations (e.g., the bottom PSFs of chip[2]).

Moreover, while for some PSFs (e.g., the one labeled as 4-(1,5) on chip[4]), we have a general decrease of the central values. For other PSFs (e.g., 1-(2,1) on chip[1]), we have a decrease of the central values during the first 15 min, followed by an increase afterwards. (Note that no focus adjustments have been made during this 34 min.)

Figure A.4 clearly shows that there are large variations in the PSF shape even from one exposure to the other, and this variation is not constant across the field. HST's PSFs are very stable

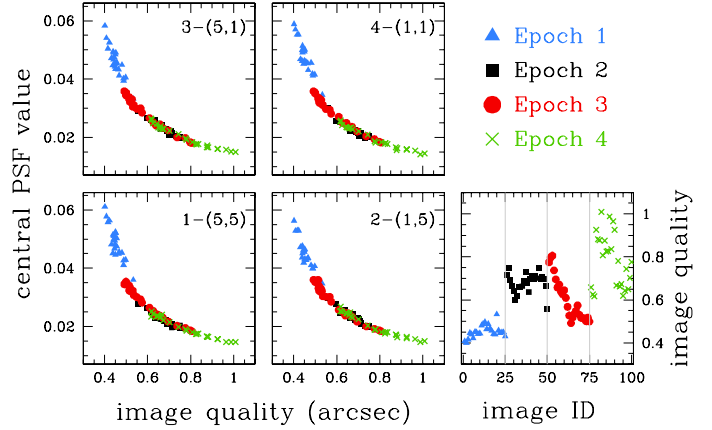


Fig. A.5. The central PSF value of these PSFs as a function of the image quality.

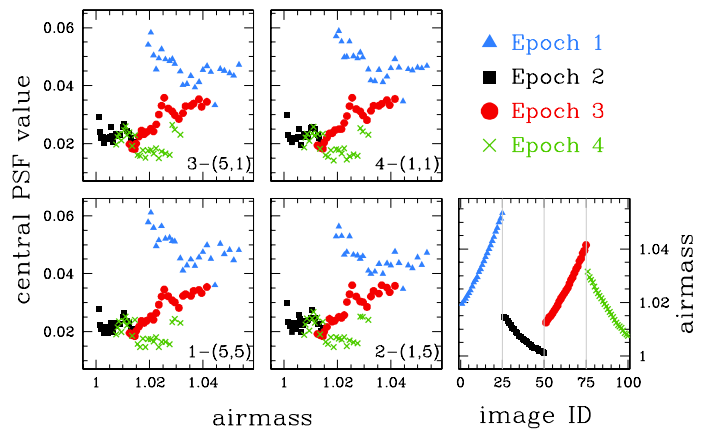


Fig. A.6. Same as Fig. A.5 but for airmass variations.

over time with variations on the order of at most a few percent, mostly due to the so-called telescope breathing<sup>8</sup>. For HST, one spatially-constant perturbation PSF for is generally enough to take into account this effect (e.g., ACS/WFC PSFs, Anderson & King 2006). To achieve high-precision astrometry and photometry with the HAWK-I camera, we have to derive a specific set of PSFs for each individual exposure.

To further infer the effects of time variation on our PSF models, we performed the following additional analysis using the 100 images in the field of M 4. As already mentioned, these images were taken in blocks of 25 consecutive exposures in four different runs, spanning three nights. Because each observing run lasted about 30 min, we can safely assume that focus variations have played a little role in changing the shape of PSFs, if compared to airmass and seeing variations. Seeing should actually be the most important factor in changing the PSF shape from one exposure to the next one. We focused on the centermost four PSFs, namely: 1-(5,5); 2-(1,5); 3-(5,1); and 4-(1,1), following labels of Fig. A.4. In Fig. A.5, we plot the central value of these PSFs as a function of the image quality (i.e., the average stars' FWHM as measured directly on the exposures). Different observing runs are marked with different colors and symbols. On the bottom right panel of the figure, we plot the variation in the

<sup>8</sup> HST focus is known to experience variations on the orbital time scale, which are attributed to thermal contraction/expansion of the HST optical telescope assembly as the telescope warms up during its orbital day and cools down during orbital night.

**Table B.1.** Size of the  $J$  corrections. All the values are given in pixels.

Chip	X-axis		Y-axis		X-axis		X-axis		X-axis		Y-axis	
	Min	Max	Min	Max	Min	Max	Min	Max	Min	Max	Min	Max
	P Correction				S Correction		FS Correction		TP Correction			
1	-2.4974	0.0001	-3.4467	0.7815	-0.0354	0.0294	-0.0922	0.0828	-0.3698	0.1842	-0.0638	0.1439
2	-0.2483	2.7147	-3.7959	0.8621	-0.0354	0.0294	-0.0221	0.0391	-0.0903	0.0602	-0.0847	0.0694
3	-2.2199	0.0001	-0.9715	3.2343	-0.0354	0.0294	-0.0197	0.0288	-0.0784	0.0979	-0.0713	0.0974
4	-0.2678	2.8462	-0.7153	3.8896	-0.0354	0.0294	-0.0323	0.0266	-0.0929	0.1281	-0.0803	0.0751

**Table B.2.** As in Table B.1 but for the  $H$  corrections (in pixels).

Chip	X-axis		Y-axis		X-axis		X-axis		X-axis		Y-axis	
	Min	Max	Min	Max	Min	Max	Min	Max	Min	Max	Min	Max
	P Correction				S Correction		FS Correction		TP Correction			
1	-2.2681	0.0001	-2.7934	0.6161	-0.0307	0.0308	-0.0365	0.0547	-0.0833	0.0643	-0.0543	0.0505
2	-0.0449	2.6406	-4.0058	0.9549	-0.0307	0.0308	-0.0188	0.0245	-0.0575	0.0497	-0.0473	0.0506
3	-2.2937	0.0001	-1.3461	3.4982	-0.0307	0.0308	-0.0328	0.0257	-0.0768	0.0920	-0.0439	0.0624
4	-0.3316	2.8668	-0.4570	3.5777	-0.0307	0.0308	-0.0298	0.0395	-0.1149	0.1084	-0.0507	0.0538

**Table B.3.** As above but for the  $K_S$  corrections (in pixels).

Chip	X-axis		Y-axis		X-axis		X-axis		X-axis		Y-axis	
	Min	Max	Min	Max	Min	Max	Min	Max	Min	Max	Min	Max
	P Correction				S Correction		FS Correction		TP Correction			
1	-2.3696	0.1417	-3.4477	0.7932	-0.0245	0.0275	-0.0661	0.0678	-0.2406	0.1095	-0.0763	0.0632
2	-0.1348	2.7460	-3.7555	0.8715	-0.0245	0.0275	-0.0146	0.0256	-0.0636	0.0557	-0.0340	0.0403
3	-2.1681	0.0001	-1.0793	3.3528	-0.0245	0.0275	-0.0272	0.0212	-0.0797	0.0799	-0.0419	0.0320
4	-0.1457	2.8005	-0.5338	3.4126	-0.0245	0.0275	-0.0152	0.0144	-0.0836	0.0532	-0.0573	0.0375

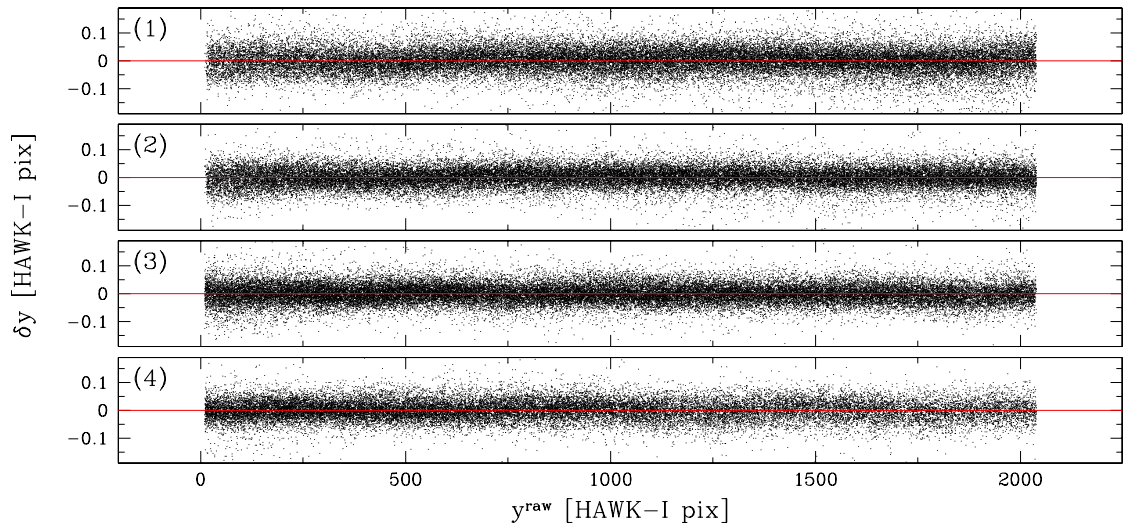
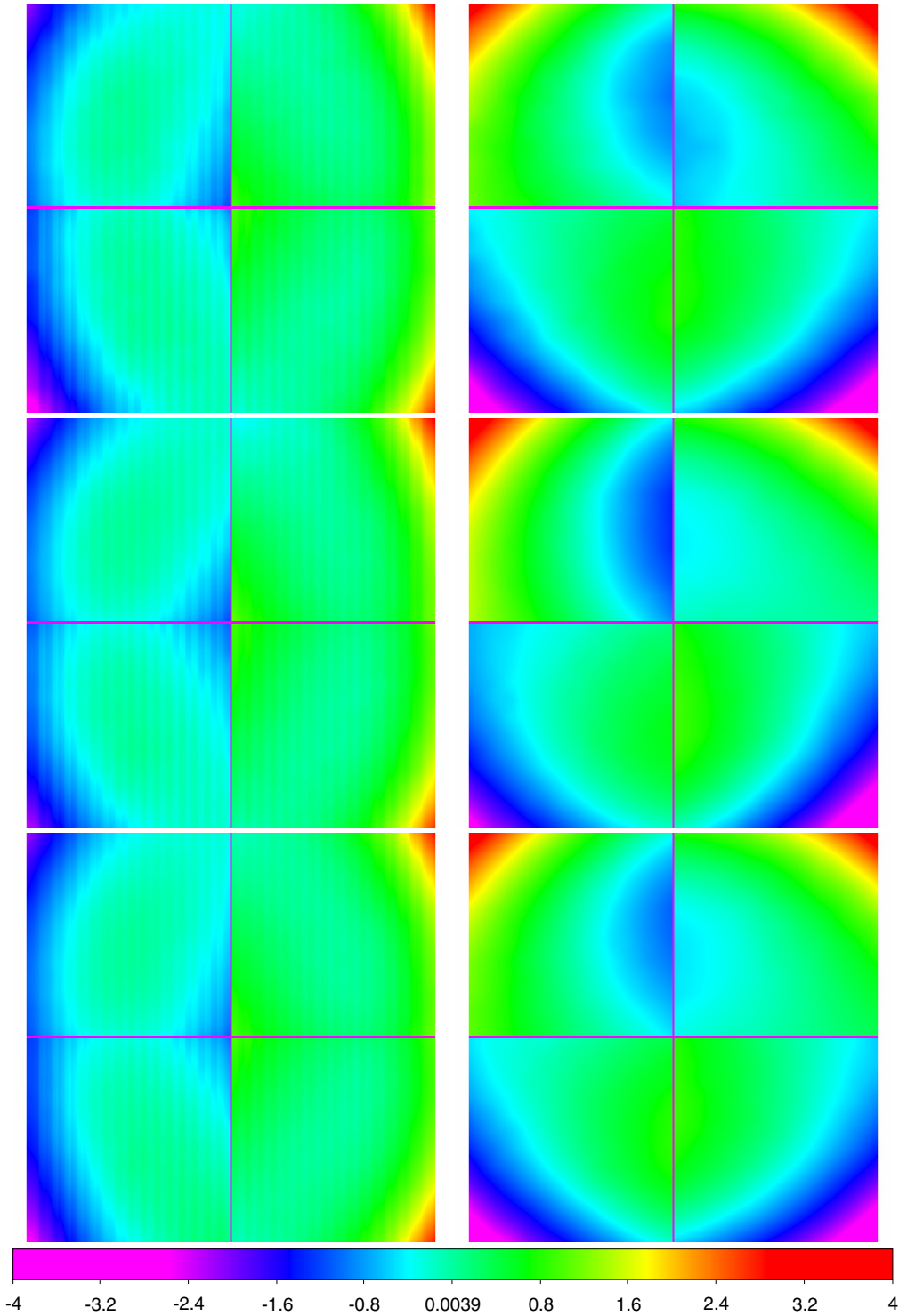

**Fig. B.1.**  $\delta y$  as function of  $Y$  in units of HAWK-I pixels for all chips. The red lines are set at 0 HAWK-I pixel.

image quality during the four runs. Here, we want to emphasize that these variations occurred within 30 min within the same run. As we expected, there is a strong correlation between our PSF shapes and image quality. The correlation between PSF shapes and airmass is shown in Fig. A.6. Airmass variations seem to play a secondary role in changing PSF shape with respect to image quality.

## Appendix B: Geometric distortion: 2D maps and size of the corrections

In this appendix, we report the size of the distortion corrections released in this paper. In Tables B.1–B.3, we show the minimum and maximum values of each correction in both coordinates for all chips. The largest correction is applied with the P corrections, which decrease from the corner to the center of the detector. The S and FS corrections are only applied to the  $x$ -coordinates. Figure B.1 demonstrates there is no  $\delta y$  periodic



**Fig. B.2.** Maps of the corrections. *From top to bottom, J-, H-, and  $K_S$ -filter corrections.* For each filter, the four chips on the *left* show the *X*-correction, while the four chips on the *right* show the *Y*-correction. A linear scale is used. Red means positive corrections; purple are negative corrections. The values in the color bar are expressed in pixels. For the *J* filter, the *x*-corrections vary between  $-2.95$  and  $2.96$  pixels across the whole detector, while the *y*-corrections vary between  $-3.88$  and  $3.95$  pixels. For the *H* filter, the minimum and maximum corrections for the *x*-coordinate are  $-2.40$  and  $2.99$  pixels, while the corrections for the *y*-coordinate are  $-4.00$  and  $3.59$  pixels. The minimum and maximum *x*-corrections for the  $K_S$ -filter solution are  $-2.67$  and  $2.85$  pixels; for *y*-corrections, the minimum and maximum are  $-3.77$  and  $3.42$  pixels.

pattern, so an FS correction along this axis is not necessary. The residual distortion is corrected with the TP correction. While the S correction is the same for all chips and has only two values, the FS correction changes from chip to chip and varies across the same chip.

In Fig. B.2, we show a 2D map of the correction for each chip/filter. In the four left boxes of each row, we plot the correction of each chip for the *x*-coordinates in the right boxes for the *y*-coordinates. The polynomial correction creates the radial pattern that changes from the corner to the center in

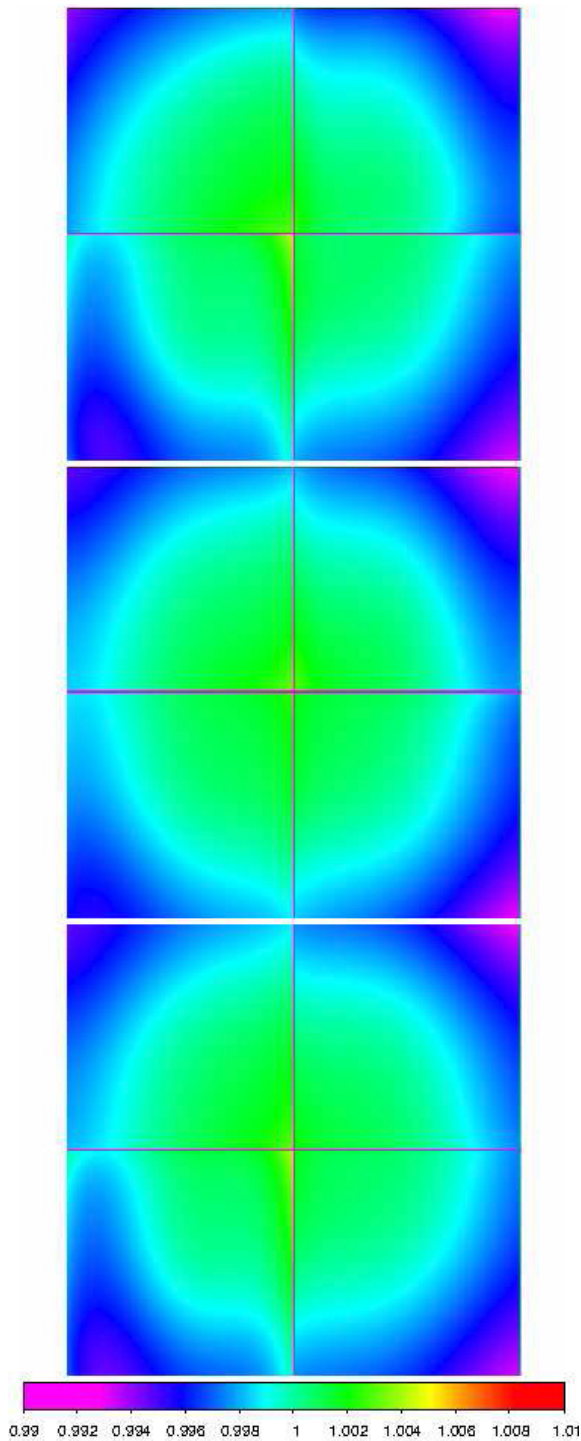


**Fig. B.3.** Maps of the pixel area corrections. From *top to bottom*,  $J$ -,  $H$ -, and  $K_S$ -filter corrections. The values in the color bar represent the corrected area of the pixels. Before the correction, all pixels have an area of  $1 \text{ pixel}^2$ . The scale in the images is linear.

all chips. The  $S$  correction is visible only in the left boxes ( $x$ -coordinate corrections) and creates a striped pattern.

Another important correction that we are going to release (as FITS images) is the correction for the pixel area variation across the detector. This is a useful tool for improving HAWK-I photometry. On average the size of the pixel area varies up to 0.7% across the detector. This value is reached at a point close to the edge and to the center of the detector. We only applied the polynomial correction, since it gives the maximum correction.

Note that the corrections of the periodic-lag effect should not be included in the pixel area correction. The periodic lag is due to charges left in the amplifiers, so the area of the pixel itself is not modified on sky. This is different to what happens with the optics+filters distortion. In Fig. B.3, we show three maps of the correction with one for each HAWK-I filter.

## References

- Anderson, J., & King, I. R. 1999, *PASP*, 111, 1095  
 Anderson, J., & King, I. R. 2003, *PASP*, 115, 113  
 Anderson, J., & King, I. R. 2004, *Instrument Science Report ACS 2004-15*, 3  
 Anderson, J., & King, I. R. 2006, *Instrument Science Report ACS 2006-01*, 1  
 Anderson, J., Bedin, L. R., Piotto, G., Yadav, R. S., & Bellini, A. 2006, *A&A*, 454, 1029 (Paper I)  
 Anderson, J., King, I. R., Richer, H. B., et al. 2008, *AJ*, 135, 2114  
 Arsenault, R., Hubin, N., Stroebels, S., et al. 2006, *The Messenger*, 123, 6  
 Bedin, L. R., Piotto, G., King, I. R., & Anderson, J. 2003, *AJ*, 126, 247  
 Bellini, A., & Bedin, L. R. 2009, *PASP*, 121, 1419  
 Bellini, A., & Bedin, L. R. 2010, *A&A*, 517, A34 (Paper IV)  
 Bellini, A., Piotto, G., Bedin, L. R., et al. 2009, *A&A*, 493, 959 (Paper III)  
 Bellini, A., Anderson, J., & Bedin, L. R. 2011, *PASP*, 123, 622  
 Golimowski, D., Suchkov, A., Loose, M., Anderson, J., & Grogan, N. 2012, *Instrument Science Report ACS 2012-02*, 2  
 Hadjyska, E., Rabinowitz, D., Baltay, C., et al. 2012, *IAU Symp.*, 285, 324  
 Han, I. 1989, *AJ*, 97, 607  
 Harris, W. E. 1996, *VizieR Online Data Catalog: VII/95*  
 Kaiser, N., Burgett, W., Chambers, K., et al. 2010, *Proc. SPIE*, 7733, 0E  
 Kaluzny, J., & Thompson, I. B. 2001, *A&A*, 373, 899  
 Kissler-Patig, M., Pirard, J.-F., Casali, M., et al. 2008, *A&A*, 491, 941  
 Kozhurina-Platais, V., Girard, T. M., Platais, I., et al. 1995, *AJ*, 109, 672  
 Lindegren, L. 1980, *A&A*, 89, 41  
 Madore, B. F., Rigby, J., Freedman, W. L., et al. 2009, *ApJ*, 693, 936  
 Milone, A. P., Stetson, P. B., Piotto, G., et al. 2009, *A&A*, 503, 755  
 Milone, A. P., Piotto, G., Bedin, L. R., et al. 2012, *A&A*, 540, A16  
 Minniti, D., Lucas, P. W., Emerson, J. P., et al. 2010, *New Astron.*, 15, 433  
 Piotto, G., Milone, A. P., Anderson, J., et al. 2012, *ApJ*, 760, 39  
 Platais, I., Kozhurina-Platais, V., Girard, T. M., et al. 2002, *AJ*, 124, 601  
 Platais, I., Wyse, R. F. G., & Zacharias, N. 2006, *PASP*, 118, 107  
 Saito, R. K., Hempel, M., Minniti, D., et al. 2012, *A&A*, 537, A107  
 Shokin, Y. A., & Samus, N. N. 1996, *Astron. Lett.*, 22, 761  
 Skrutskie, M. F., Cutri, R. M., Stiening, R., et al. 2006, *AJ*, 131, 1163  
 Stetson, P. B. 1987, *PASP*, 99, 191  
 Stetson, P. B. 2000, *PASP*, 112, 925  
 Stetson, P. B. 2005, *PASP*, 117, 563  
 van Altena, W. F. 2013, *Astrometry for Astrophysics*, ed. W. F. van Altena (Cambridge: Cambridge University Press)  
 Yadav, R. K. S., Bedin, L. R., Piotto, G., et al. 2008, *A&A*, 484, 609 (Paper II)  
 Zacharias, N., Finch, C. T., Girard, T. M., et al. 2013, *AJ*, 145, 44  
 Zloczewski, K., Kaluzny, J., Rozyczka, M., Krzeminski, W., & Mazur, B. 2012, *Acta Astron.*, 62, 357